The Astrophysical Journal, 915:70 (19pp), 2021 July 1 https://doi.org/10.3847/1538-4357/abfc52

WALLABY Pilot Survey: The Diversity of Ram Pressure Stripping of the Galactic H I Gas in the Hydra Cluster

Jing Wang (王菁)[1], Lister Staveley-Smith[2,3], Tobias Westmeier[2,3], Barbara Catinella[2,3], Li Shao (邵立)[4], T. N. Reynolds[2,3], Bi-Qing For[2,3], Bumhyun Lee[1], Ze-zhong Liang (梁泽 众)[5], Shun Wang (王舜)[1,5], A. Elagali[6], H. Dénes[7], D. Kleiner[8], Bärbel S. Koribalski[9,10], K. Lee-Waddell[2,11], S-H. Oh[12], J. Rhee[2,3], P. Serra[8], K. Spekkens[13], O. I. Wong[2,3,11], K. Bekki[2,3], F. Bigiel[14], H. M. Courtois[15], Kelley M. Hess[16,17], B. W. Holwerda[18], Kristen B. W. McQuinn[19], M. Pandey-Pommier[20], J. M. van der Hulst[21], and L. Verdes-Montenegro[22]

[1] Kavli Institute for Astronomy and Astrophysics, Peking University, Beijing 100871, People's Republic of China; jwang_astro@pku.edu.cn
[2] International Centre for Radio Astronomy Research, University of Western Australia, 35 Stirling Highway, Crawley, WA 6009, Australia
[3] ARC Centre of Excellence for All-Sky Astrophysics in 3 Dimensions (ASTRO 3D), Australia
[4] National Astronomical Observatories, Chinese Academy of Sciences, 20A Datun Road, Chaoyang District, Beijing, People's Republic of China
[5] Department of Astronomy, School of Physics, Peking University, Beijing 100871, People's Republic of China
[6] Telethon Kids Institute, Perth Children's Hospital, Perth, Australia
[7] ASTRON—The Netherlands Institute for Radio Astronomy, 7991 PD Dwingeloo, The Netherlands
[8] INAF—Osservatorio Astronomico di Cagliari, Via della Scienza 5, I-09047 Selargius (CA), Italy
[9] Australia Telescope National Facility, CSIRO Astronomy and Space Science, P.O. Box 76, NSW 1710, Epping, Australia
[10] Western Sydney University, Locked Bag 1797, Penrith, NSW 2751, Australia
[11] CSIRO Astronomy and Space Science (CASS), PO Box 1130, Bentley, WA 6102, Australia
[12] Department of Physics and Astronomy, Sejong University, 209 Neungdong-ro, Gwangjin-gu, Seoul, Republic of Korea
[13] Royal Military College of Canada, PO Box 17000, Station Forces, Kingston, Ontario, K7K7B4, Canada
[14] Argelander-Institut für Astronomie, Universität Bonn, Auf dem Hüugel 71, D-53121 Bonn, Germany
[15] Université de Lyon, Université Claude Bernard Lyon 1, IUF, IP2I Lyon, F-69622, Villeurbanne, France
[16] ASTRON, the Netherlands Institute for Radio Astronomy, Postbus 2, 7990 AA, Dwingeloo, The Netherlands
[17] Kapteyn Astronomical Institute, University of Groningen, P.O. Box 800, 9700 AV Groningen, The Netherlands
[18] University of Louisville, Department of Physics and Astronomy, 102 Natural Science Building, 40292 KY Louisville, USA
[19] Rutgers University, Department of Physics and Astronomy, 136 Frelinghuysen Road, Piscataway, NJ 08854, USA
[20] University Claude Bernard Lyon 1, 43 Boulevard du 11 Novembre 1918, F-69100 Villeurbanne, France
[21] Kapteyn Astronomical Institute, University of Groningen, The Netherlands
[22] Instituto de Astrofísica de Andalucía (CSIC), Spain
Received 2021 March 17; revised 2021 April 20; accepted 2021 April 26; published 2021 July 7

Abstract

This study uses H I image data from the Widefield ASKAP L-band Legacy All-sky Blind surveY (WALLABY) pilot survey with the Australian Square Kilometre Array Pathfinder (ASKAP) telescope, covering the Hydra cluster out to $2.5r_{200}$. We present the projected phase–space distribution of H I-detected galaxies in Hydra, and identify that nearly two-thirds of the galaxies within $1.25r_{200}$ may be in the early stages of ram pressure stripping. More than half of these may be only weakly stripped, with the ratio of strippable H I (i.e., where the galactic restoring force is lower than the ram pressure in the disk) mass fraction (over total H I mass) distributed uniformly below 90%. Consequently, the H I mass is expected to decrease by only a few 0.1 dex after the currently strippable portion of H I in these systems has been stripped. A more detailed look at the subset of galaxies that are spatially resolved by WALLABY observations shows that, while it typically takes less than 200 Myr for ram pressure stripping to remove the currently strippable portion of H I, it may take more than 600 Myr to significantly change the total H I mass. Our results provide new clues to understanding the different rates of H I depletion and star formation quenching in cluster galaxies.

Unified Astronomy Thesaurus concepts: Disk galaxies (391); Galaxies (573); Interstellar atomic gas (833); Galaxy evolution (594); Galaxy environments (2029)

1. Introduction

Galaxies evolve in their morphologies, kinematics and stellar population, a process that is accelerated when they are in clusters (Boselli & Gavazzi 2006). Neutral atomic hydrogen (H I) is a major part of the interstellar medium in a galaxy (e.g., Catinella et al. 2018; Wang et al. 2020a) and is a crucial component in the kinematic and thermal cooling of baryons (Putman et al. 2012). It is also an important step in the baryonic mass flow and therefore an important key for understanding galaxy evolution. Clusters provide an environment where gravitational and hydrodynamic effects efficiently remove the H I in their constituent galaxies (e.g., Boselli & Gavazzi 2006; Stevens et al. 2019), with ram pressure stripping (RPS) identified as one of the most important mechanisms at low redshift.

Based on the analytical model of Gunn & Gott (1972), the strength of RPS can be quantified by comparing the ram pressure from the intra-cluster medium (ICM) against the localized gravitational anchoring force of the galactic disk. We can thus expect that there is a diversity in the ways that galaxies experience RPS, as infalling galaxies have different distributions of mass and gas, and travel along different orbits and with different disk inclinations against the ICM wind. Hydrodynamical simulations of cluster systems confirm these complexities (Abadi et al. 1999; Vollmer et al. 2001; Roediger & Brüggen 2006, 2007; Jáchym et al. 2009; Bekki 2014; Lotz et al. 2019; Tonnesen 2019) and further elaborate on the influence of other factors such as the

multiphase nature of gas (Tonnesen & Bryan 2009, 2010; Lee et al. 2020; Stevens et al. 2020), magnetic fields (Tonnesen & Stone 2014; Ramos-Martínez et al. 2018), and substructures in clusters (Tonnesen & Bryan 2008; Ruggiero et al. 2019). Probing the observational dependence of RPS on galaxy properties requires statistically mapping the H I in cluster galaxies with high resolution. RPS is also studied with other tracers like the ionized gas (Jaffé et al. 2018) and the radio continuum (Chen et al. 2020), but this paper focuses on the RPS of H I, which is the reservoir for star formation.

Galaxies displaying H I tails that resemble expected RPS morphologies have been identified in nearby clusters (e.g., Kenney et al. 2004; Chung et al. 2007, 2009; Koribalski 2020b). The shape, length, and column density of those H I tails provide information regarding the progress of gas removal, orbits of infall, time since infall, and local ICM structures, particularly when they are combined with multiwavelength information like the star formation rate (SFR; Vollmer et al. 2012; Jaffé et al. 2016), gas in other phases (Abramson et al. 2011; Lee et al. 2017; Moretti et al. 2020), dust (Crowl et al. 2005), radio polarization (Vollmer et al. 2013), and numerical simulations (Vollmer et al. 2001; Tonnesen & Bryan 2010). Statistically, RPS provides a good explanation for the observed distributions of SFRs and H I richness in clusters, including trends as a function of the cluster-centric projected distance (Gavazzi et al. 2006; Woo et al. 2013; Hess et al. 2015), cluster-centric radial velocity offset (Mahajan et al. 2011; Jaffé et al. 2015), and galactic stellar mass (Zhang et al. 2013). However, detailed studies of resolved systems have been mostly limited to a few systems, while statistical studies have mostly been based on spatially unresolved H I data.

Contiguously mapping the H I in clusters is essential to bridge the gap between signatures of RPS in individual galaxies and the role that RPS plays in cosmological galaxy evolution. The need for a cosmological context is because the majority of the galaxies infalling for the first time into massive clusters may have been preprocessed as satellites (Fujita 2004; Cybulski et al. 2014; Bahé et al. 2019), or undergone *mass quenching* as centrals (Kauffmann et al. 2003) in less massive groups. It has been found that the timescale for quenching the SFR anticorrelates with the stellar mass of satellite galaxies, not because the more massive galaxies are more vulnerable to the current environment, but because they were fully or partly preprocessed or mass quenched for a longer time in their previous environments (De Lucia et al. 2012; Wetzel et al. 2013; Oman & Hudson 2016; Rhee et al. 2020). It has also been found that 20%–50% of low-mass satellite galaxies may have already or partly been quenched in star formation, with gas depleted to some extent, in another dark matter halo before being accreted into the current cluster (Hess & Wilcots 2013; Wetzel et al. 2013; Haines et al. 2015; Jung et al. 2018). The galactic properties shaped by the past evolution strongly affect the strength and importance of environmental processing in the current cluster (Jung et al. 2018). A complete census of cluster galaxies is needed in order to properly account for the diversity of initial conditions at infall.

However, it has been hard to achieve both high completeness and high resolution in H I observations for clusters, mostly because covering a large area with interferometric 21 cm observations has been unfeasible. Extensive statistical studies based on more complete samples of galaxies detected in the nearby clusters Virgo, Coma, A1367, and others have been conducted using H I data from blind single dish H I surveys, particularly The Arecibo Legacy Fast ALFA (ALFALFA; Haynes et al. 2018) and HI Parkes All Sky Survey (HIPASS; Meyer et al. 2004). They provide the benchmark for integral properties of H I in massive clusters, including the major scaling relations (Cortese et al. 2008, 2011; Dénes et al. 2014; Odekon et al. 2016) and mass functions (Gavazzi et al. 2006; Jones et al. 2016). Interferometric H I images of selected galaxies from these H I samples were also obtained to gain details about ongoing physical processes (Warmels 1988; Gavazzi 1989; Cayatte et al. 1990; Scott et al. 2010, 2018). Among them, the VLA Imaging of Virgo in Atomic gas (VIVA) targeted survey of 50 late-type galaxies in the Virgo cluster (Chung et al. 2009) has been one of the largest resolved data sets. Further away, the Blind Ultra Deep HI Survey (BUDHIES) mapped two clusters (Jaffé et al. 2015) at relatively high redshifts ($z \sim 0.2$) out to $3r_{200}$ (where r_{200} is the radius within which the averaged density is 200 times the critical density of the universe) with interferometry, with poorer resolution, and mass sensitivity. Wang et al. (2020b) thus used the predicted H I radial distributions, in order to better exploit the low-resolution, wide-field H I data. Based on a relatively complete overlap between the ROSAT X-ray survey and the ALFALFA H I survey, for 26 massive clusters and around 200 galaxies, they showed that the RPS of the H I outer disks is prevalent out to $1.5r_{200}$ in Coma-like clusters, pointing out the potentially important role of weak RPS on galaxy evolution in clusters.

Taking advantage of the high survey efficiency of the Australian Square Kilometre Array Pathfinder (ASKAP), the pilot survey of Widefield ASKAP L-band Legacy All-sky Blind surveY (WALLABY[23]; Koribalski et al. 2020a) has been targeting nearby clusters and groups. In this study, we use its second internal data release of the Hydra cluster.[24]

As we will show in this paper, WALLABY is biased against galaxies with H I masses less than a few times $10^8\,M_\odot$ at the distance of Hydra. Galaxies with stellar masses below around $10^9\,M_\odot$ may therefore not appear in the WALLABY catalog if they are highly H I deficient (Section 4), which are the most commonly used samples for RPS studies (e.g., Boselli et al. 2014). But the data fully cover the Hydra cluster out to $2r_{200}$ (Section 3), and provide resolved H I distributions in a few galaxies, which we use as the test sample for predicting the H I distribution in the unresolved galaxies (Section 2.3.2). Based on this, we attempt to quantify the instantaneous speed of H I depletion due to RPS in the detected galaxies by quantifying the level of ram pressure, anchoring force, and mass of strippable H I. The analysis thus provides statistics about the acceleration and speed of cluster processing through RPS at a relatively early stage of H I depletion (i.e., before the H I deficiency level becomes high, as the sample is strongly biased toward H I-rich galaxies). Although we do not know the initial conditions of galactic H I masses or distributions upon infall (passing $2r_{200}$), the WALLABY coverage provides us with a snapshot of cluster processing, giving insight into the role of RPS in removing H I from galaxies infalling into massive clusters. Observationally this is the first major study of a cluster beyond the local Virgo, Coma, and A1367 clusters. The most extensively studied of these, Virgo, is not representative of clusters with similar masses as it is dynamically unrelaxed (Boselli et al. 2014). Furthermore, Virgo has an ICM that is

[23] https://wallaby-survey.org/
[24] https://research.csiro.au/casda/

more centrally concentrated compared to a dynamically mature cluster (Roediger & Brüggen 2007).

Hydrodynamic (Bahé et al. 2013; Bahé & McCarthy 2015; Jung et al. 2018; Bahé et al. 2019; Lotz et al. 2019; Ayromlou et al. 2021; Stevens et al. 2020; Oman et al. 2021) and semi-analytical (Luo et al. 2016; Stevens & Brown 2017; De Lucia et al. 2019; Stevens et al. 2019; Xie et al. 2020) models have made progress in recent years narrowing the differences between predicted and observed distribution of H I density within galaxies and scaling relations of H I mass in galaxies. However, because galaxies are complex systems, many different mechanisms produce a similar trend (Stevens & Brown 2017). So far as we know, after the early works of Vollmer et al. (2001), Boselli et al. (2014), and others for the Virgo cluster galaxies, there has been very few observational studies that directly provide the full distribution of the ram pressure/restoring forces and the mass of strippable H I for all the detected galaxies in the cluster. This is needed to separate the amount of gas loss due to RPS from that due to feedback or star formation. Furthermore, resolved H I images are preferable to simple catalogs of H I detections. As we show in the paper (Section 2.3.2), the radial distribution of H I in cluster galaxies differs from that of galaxies in the field, though they do obey the same size–mass relation (Wang et al. 2016; Stevens et al. 2019). As a result we apply a correction factor to the fraction of instantaneous strippable H I mass predicted with the typical radial profile of H I of field galaxies. Obviously one individual cluster is not enough to provide strong constraints to cosmological simulations, but the analysis presented in this paper can be extended with future WALLABY observations covering multiple clusters.

The outline of this paper is as follows. We present the data in Section 2, discuss the phase–space distribution of H I-detected galaxies and RPS affected galaxies in Section 3, the distribution of H I richness and RPS strength in Section 4, the timescales for RPS to remove the currently affected H I and the existing H I reservoir in Section 5. We assume a Lambda cold dark matter cosmology, with $\Omega_m = 0.3$, $\Omega_\lambda = 0.7$, and $h = 0.7$. We assume the Chabrier (2003) initial mass function when estimating the stellar mass.

2. Data and Methodology

2.1. Data

The Hydra cluster has a distance of 47.5 ± 3 Mpc, a center at $\alpha = 159.^\circ0865$ and $\delta = -27.^\circ5629$, and a heliocentric velocity of 3686 km s^{-1} (Kourkchi & Tully 2017). Analysis based on X-ray data suggested a characteristic radius $r_{200} \sim 1.35$ Mpc, and the mass within this radius, $M_{200} \sim 3.02 \times 10^{14}\, M_\odot$ (Reiprich & Böhringer 2002). Its velocity dispersion $\sigma_C = 620$ km s^{-1} is derived from M_{200} using the equation of Evrard et al. (2008). The Hydra cluster is a dynamically highly mature system, with a smooth X-ray halo and little substructure (Fitchett & Merritt 1988; Lima-Dias et al. 2021). There is a hint of two or three substructures in velocity near the cluster center (within $0.4r_{200}$, Fitchett & Merritt 1988), but on the whole Hydra is dynamically much more settled than the Virgo cluster. The Hydra cluster is connected to the Antlia cluster via a filament, and the latter was mapped in H I by the Karoo Array Telescope (KAT-7) with a mosaic of 4.4 deg^2 (Hess et al. 2015).

WALLABY mapped a 60 deg^2 area around its center, reaching out to $4r_{200}$ and fully covering the region within $2r_{200}$. The WALLABY observation reached a targeted sensitivity of $\sigma_{\rm cube} = 2.0 \pm 0.5$ mJy beam^{-1}, with a circular beam FWHM of $b_{\rm maj} \sim 30''$ (∼7 kpc at the distance of Hydra) and a velocity spectral resolution of 4 km s^{-1}. The raw data was reduced with ASKAPsoft (Whiting 2020), and H I sources were extracted using SoFiA 2[25] with a multi-kernel smooth+clip algorithm (Serra et al. 2015) at a significance level of 3.5σ. Details about the observation, data reduction, and source finding are discussed in earlier WALLABY publications (Elagali et al. 2019; For et al. 2019; Kleiner et al. 2019; Lee-Waddell et al. 2019; Koribalski et al. 2020a). More details of the data used in this paper will be further elaborated in T. Westmeier et al. (2021, in preparation). In this analysis we focus on the detections ($N = 105$) with projected distances within $2.5r_{200}$ and radial velocity differences within the upper limit of the escape velocity from the cluster center. We highlight an H I overview of this phase–space region around the Hydra center in Figure 1.

We use the optical g- and r-band images from the second data release of Pan-STARRS (Waters et al. 2020) to derive optical properties. We use the photometric pipeline described in Wang et al. (2017, 2018), which includes standard procedures of background removal, masking, segmentation, and flux measurements. We use Kron magnitudes and the radial profiles of the surface brightness. We correct for the Galactic extinction using the IRSA Dust Extinction Service. We use the formula of Zibetti et al. (2009) to calculate the r-band stellar mass to light ratio based on the $g - r$ color (assuming the Chabrier 2003 initial mass function), and estimate the stellar mass M_* based on the r-band luminosity.

We exclude nine systems that are likely to be strongly tidally interacting, have highly irregular optical and H I morphologies, or have H I bridges connecting two or multiply major galactic systems. We also exclude seven galaxies that do not have good optical images from Pan-STARRS, leaving 89 galaxies in our main sample.

Although we attempted to exclude major merger candidates, we cannot exclude the influence from gravitational effects, including the harassment from surrounding galaxies (Moore et al. 1996, 1998) and the tidal force from the main cluster (Byrd & Valtonen 1990). Simulations suggests that, in addition to directly stripping the gas (Merritt 1983; Łokas 2020) and inducing gas inflows (Byrd & Valtonen 1990; Blumenthal & Barnes 2018; Moreno et al. 2019; Patton et al. 2020), gravitational effects may assist RPS by enhancing local ICM density (Markevitch & Vikhlinin 2007; Bekki et al. 2010; Roediger et al. 2011; McPartland et al. 2016) and relative velocities (Ruggiero et al. 2019), and moving H I to regions of lower anchoring force (Kapferer et al. 2008). There can be other hydrodynamic effects from the environment like viscous stripping (Nulsen 1982), but in this study we focus on the effect of RPS.

2.2. The Ram Pressure Level

We largely follow the procedure of Wang et al. (2020b) to estimate the ram pressure and the anchoring force. We use the equation from Ettori (2015) to convert the cluster dynamic mass to ICM mass, and then convert the double-beta model of the X-ray surface brightness radial profile (from Eckert et al. 2011) to the ICM number density ($n_{\rm ICM}$) profile as a function of

[25] https://github.com/SoFiA-Admin/SoFiA-2

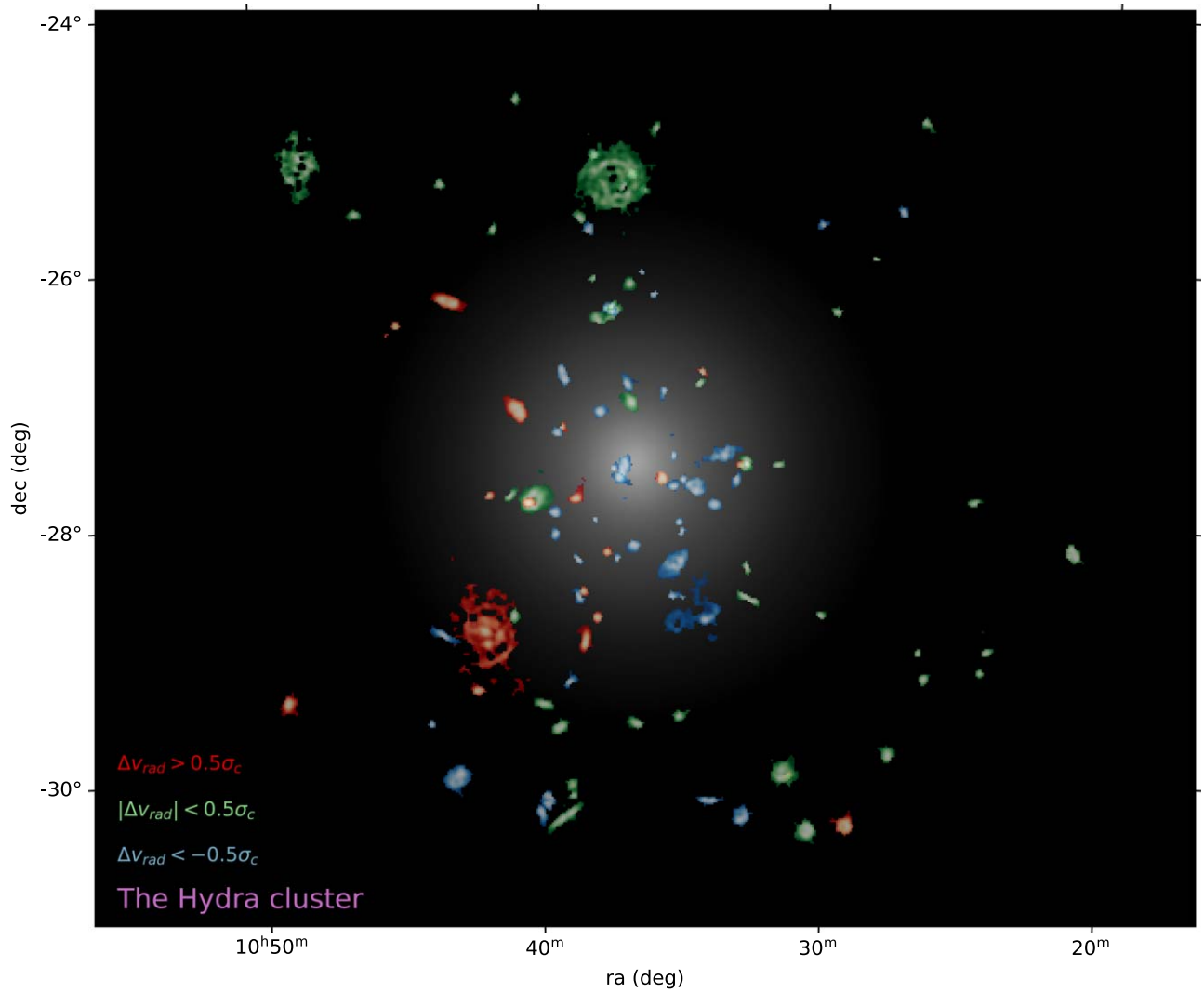

Figure 1. WALLABY-detected galaxies in the Hydra cluster. The frame is $5.5r_{200}$ in width and $4.5r_{200}$ in height, where r_{200} is the cluster-centric radius where the enclosed averaged density is 200 times the cosmological critical density. The H I column density images are shown in different slices of velocity offset from the cluster center ($\Delta v_{\rm rad}$) around the X-ray halo of Hydra (gray scale, based on the ICM model described in Section 2.2). The column density images are enlarged by a factor of 5 for clarity. A similar image has been shown for the Virgo Cluster by Chung et al. (2009) using targeted H I observations.

the cluster-centric radius r:

$$n_{\rm ICM}(r)/\ {\rm cm}^{-3} = 0.003(1 + (r/0.101\ {\rm Mpc})^2)^{-1} + 0.004(1 + (r/0.027\ {\rm Mpc})^2)^{-1}. \quad (1)$$

The ram pressure is estimated as $P_{\rm ram} = \rho(d_{\rm proj})\ \Delta v_{\rm rad}^2$ (Gunn & Gott 1972), where $\rho(d_{\rm proj}) = 1.4 m_p n_{\rm ICM}(d_{\rm proj})$, m_p is the mass of proton and 1.4 accounts for mass contribution from the helium, $d_{\rm proj}$ is the projected distance from the cluster center, and $\Delta v_{\rm rad}$ is the velocity difference from the cluster center. Because the observed $\Delta v_{\rm rad}$ and $n_{\rm ICM}(d_{\rm proj})$ are lower and upper limits of the real relative velocity and the ICM density, their underestimating and overestimating effects to some extent cancel out in the estimate of $P_{\rm ram}$, mitigating the uncertainties from projection effects.

There may be additional uncertainties related to the assumptions of the isothermal and smooth nature of the ICM distribution and the extrapolation of the ICM profile. These effects should be of lower importance than projection effects, as Hydra is a dynamically relaxed cluster.

2.3. Quantifying the Strippable H I

The anchoring force (or restoring force) is estimated with a modified equation of the Gunn & Gott (1972) model, as

$$F_{\rm anchor} = 2\pi G(\Sigma_* + \Sigma_{\rm HI})\Sigma_{\rm HI}, \quad (2)$$

where G is the gravitational constant, and Σ_* and $\Sigma_{\rm HI}$ are localized stellar and H I surface densities (projection corrected) within the galaxy. Below we describe two parallel methods of calculating $F_{\rm anchor}$ and thereafter quantifying the RPS strength by comparing $F_{\rm anchor}$ with $P_{\rm ram}$. The first method makes use of H I images and is most accurate for the resolved galaxies. The second method makes use of predicted H I radial distributions and works for the whole main sample. We will use results (e.g., identification of RPS candidates, estimate of the strippable H I mass) from the first method to check the reliability of results from the second method.

2.3.1. Quantifying the Strippable H I with H I Moment-0 Images

We only consider the pixels of H I intensity images with a column density $>10^{20}\ {\rm cm}^{-2}$, corresponding to a threshold of

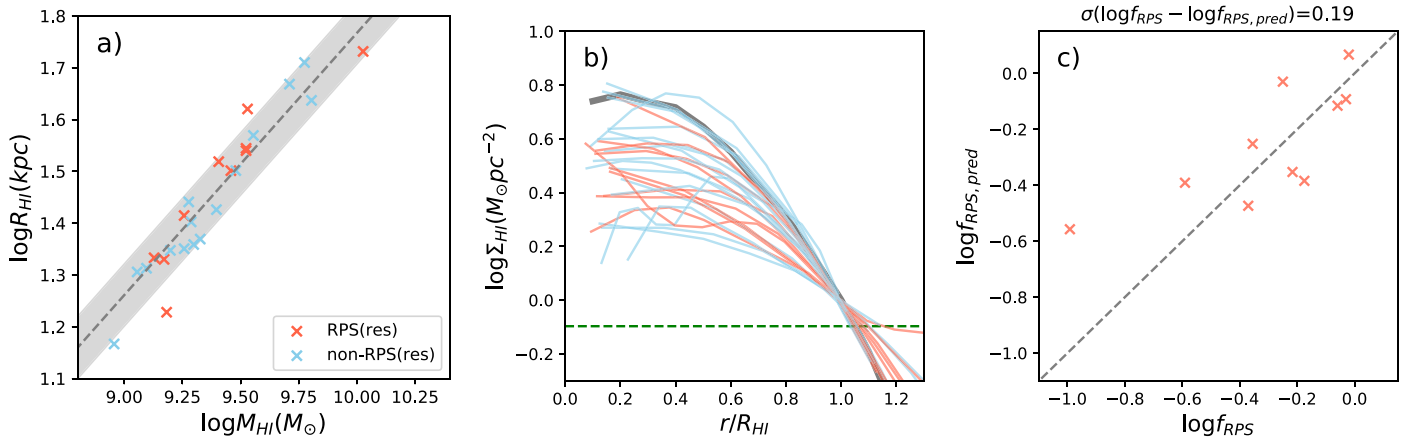

Figure 2. Radial measurements of H I for the 27 well-resolved galaxies. Panel (a): the size–mass relation of H I. The sizes $R_{\rm HI}$ have been corrected for the effect of beam smearing as $R_{\rm HI} = \sqrt{R^2_{\rm HI,obs} - b^2_{\rm maj}}$, where $R_{\rm HI,obs}$ is directly derived from the H I images as the semimajor axis of the ellipse with a de-projected surface density of 1 $M_\odot$ pc^{-2}. The mean relation and scatter from Wang et al. (2016) is plotted as the gray line and shaded region. Panel (b): the radial profiles of the H I surface density $\Sigma_{\rm HI}$. The projection correction has been applied assuming an infinitely thin disk and an axis ratio determined from the optical light. The radii are normalized by $R_{\rm HI}$. The median profile of 168 late-type galaxies (Wang et al. 2016, 2020a) is plotted as a gray, thick curve. The green dashed line marks $\Sigma_{\rm HI} = 0.8\,M_\odot$ corresponding to the detection limit of the WALLABY data. Panel (c): predicted vs. observed fraction of strippable H I mass over the total H I mass ($f_{\rm RPS}$) for the resolved-RPS candidates. The predicted fraction $f_{\rm RPS,pred}$ has been corrected by multiplying by a factor of 1.4 (see text), in order to match the observed $f_{\rm RPS}$ on the one-to-one line. The 1σ rms of the difference between the two quantities are 0.19 dex, which drops to 0.14 dex if we exclude the one outlier which has $f_{\rm RPS}$ close to the threshold of 0.1 for identifying RPS candidates. In all panels, RPS (non-RPS) candidates are in red (blue).

$2\sigma_{\rm cube}$ with a velocity width of 20 km s^{-1}. The H I disks with an area larger than 6.2 times the beam area are considered resolved and others the unresolved disks. The threshold of 6.2 beam areas is equivalent to requiring a circle with the same area to have a radius $>1.5b_{\rm maj}$, as the beam area is estimated as 1.134 $b^2_{\rm maj}$. We use each of the pixels to estimate $\Sigma_{\rm HI}$ in a resolved H I disk and only use the pixel with the peak value in an unresolved H I disk in order to have a conservative, high-limit estimate of $F_{\rm anchor}$. We extrapolate the stellar mass density exponential profiles to match the radial extension of the H I disks. We correct both H I and stellar surface densities for projection effects by multiplying them by the optical axis ratio, assuming infinitely thin disks. We caution that, the inner $\Sigma_{\rm HI}$ can be both overestimated and underestimated when the galaxies are marginally resolved. A general approach needs to be devised in the future to correct for these beam smearing effects. By using the stellar mass density profiles instead of two-dimensional distributions, we may average out outlying structures like faint spiral arms and cause a local under or over-estimate of the anchoring forces, but it is the most reliable way to derive Σ_* in the low signal-to-noise ratio outer disks.

We compare the ram pressure with the anchoring force to estimate the fraction of H I flux under stripping within a disk. For a resolved H I disk, we first produce an initial binary map for ram pressure stripped pixels with lower anchoring force than the ram pressure. We then undertake an *erode* and *dilate* process to remove unreliable pixels at the edge of disks and to ensure that the ram pressure stripped region covers at least one independent beam, which is 5 pixels across. This is done with two iterations of each operation using the Python package scipy.ndimage. Such a treatment results in an identification bias against ram pressure stripped pixels along the minor axis of disks, but ensures a relatively conservative identification. We use this binary map to compute the fraction of H I flux being stripped, $f_{\rm RPS}$. We consider those galaxies with $f_{\rm RPS} > 0.1$ as undergoing RPS (referred to as RPS candidates). We refer to the resolved galaxies that have $f_{\rm RPS} < 0.1$ as the non-RPS candidates. By doing so, we attempt to catch the galaxies at an early stage of continuous stripping, and do not include the galaxies that were already severely stripped in the past, left with a heavily truncated disk of H I incapable of being stripped any more, and are extremely H I deficient at the present. We show later in Section 2 that the sample is strongly biased toward H I-rich galaxies and more suitable to study the former type of galaxies than the latter.

Because we only consider the peak pixel, $f_{\rm RPS}$ is either 1 or 0 for an unresolved H I disk. We note that $f_{\rm RPS}$ for these unresolved RPS candidates are only used for marking them as RPS candidates but not further analyzed.

The fraction of strippable H I ($f_{\rm RPS}$) is of course an underestimate as some H I will have already left the galaxy and no longer visible. Indeed, with $f_{\rm RPS}$ we do not attempt to quantify the exact amount of stripped H I under the current or past ram pressure, but instead use it as an indicator for the instantaneous H I loss rate due to RPS (or an indicator for the stripping strength). Two assumptions have been made when $f_{\rm RPS}$ is interpreted in this way: the length of time for ram pressure to accelerate and remove a strippable H I cloud cannot be ignored, and the length of time for ram pressure to deplete the whole H I disk is relatively long compared to the removal of a strippable cloud. We show in Section 5 that both assumptions are reasonable for at least the resolved galaxies.

In total, there are 27 resolved H I disks, among which 10 are identified to be potentially under RPS. As can be seen in Figure 2(c), the majority of the RPS candidates have $f_{\rm RPS} > 0.25$, so the sample and related results do not change much if we raise the criterion for identifying RPS candidates to $f_{\rm RPS} > 0.2$. From the H I and RPS atlas of these 10 resolved-RPS candidates (Figure 10 in the Appendix), many of them display lopsidedness with respect to the optical disks, indicative of ram pressure stripped tails. We do not clearly observe tails in most of the galaxies, possibly because of the limited resolution ($\sim$7 kpc) and depth (10^{20} cm^{-2}) of the data. On the other hand, the difficulty of identifying morphological features in weak RPS galaxies has been previously pointed out in hydrodynamic simulations (Jung et al. 2018). We find that

those tentative tails (or lopsidedness) do not always point away from the center of Hydra, which may result from the combined projection effect of the viewing angle and the disk orientation with respect to the orbits. The randomness in orientation of ram pressure stripped tails was also noticed in the literature, both in observations (e.g., Kenney et al. 2014) and in hydrodynamic simulations (Yun et al. 2019). Additionally, there are 13 unresolved RPS candidates.

There are also several sources of uncertainties in the estimate of $F_{\rm anchor}$, including the neglect of stellar bulges, dark matter halos, and circumgalactic medium, and most importantly the assumption of face-on infall orientations. Uncertainties due to the neglect of the different galactic components are mitigated by the fact that the H I-rich galaxies tend to have small bulges, and the high mass of Hydra tends to truncate dark matter halos and remove the circumgalactic medium from galaxies (Bahé et al. 2013; Bahé & McCarthy 2015). Uncertainties due to the assumption of face-on infall are mitigated by previous hydrodynamic simulation results that orientations do not significantly affect H I mass loss due to RPS unless the galaxies infall nearly edge-on (inclination $>60°$, Roediger & Brüggen 2006). Nevertheless, given all these potential uncertainties, we caution that all results from the RPS analysis in this paper should be understood in a statistical sense.

2.3.2. Quantifying the Strippable H I with Predicted H I Radial Distributions

Since, as mentioned in the last section, when the H I disks are spatially unresolved we can only identify the strongly stripped galaxies, we also use the method of Wang et al. (2020b) based on the H I size–mass relation to identify RPS candidates in the main sample. We use the H I size–mass relation to estimate the radius $R_{\rm HI}$, where the H I surface density is $\Sigma_{\rm HI} \sim 1\,M_{\odot}\,{\rm pc}^{-2}$ (Wang et al. 2016). We confirm in Figure 2(a) that at least for the resolved galaxies, the size–mass relation still holds in the Hydra cluster, consistent with the theoretical predictions of Stevens et al. (2019). We then compare the ram pressure with the anchoring force at $R_{\rm HI}$ for each galaxy, and identify the RPS candidates (the r1-RPS candidates hereafter). We identify 40 r1-RPS candidates from the whole main sample. We check the reliability of r1-RPS identification in the bottom panel of Figure 3, by overplotting the r1-(non-)RPS and (non-)RPS candidates. The r1-RPS identification is highly consistent with that based on H I images when the disks are resolved. Particularly, all the RPS (resolved and unresolved) candidates are successfully identified as r1-RPS candidates, and only one non-RPS candidates is mistakenly identified as an r1-RPS candidate. This galaxy (NGC 3336, WALLABY J104016-274630) has a strong bar and spiral arms, which might have concentrated the H I into a bright ring in the inner disk and caused the deviation of the real $R_{\rm HI}$ from the predicted one.

Because different galaxies have similar profiles of $\Sigma_{\rm HI}$ as a function of $r/R_{\rm HI}$ in the outer region (Wang et al. 2016), we use the median profile of 168 late-type galaxies from Wang et al. (2016) to estimate the H I stripping fraction $f_{\rm RPS,pred}$ for the r1-RPS candidates. For each galaxy, we have used the size–mass relation to estimate $R_{\rm HI}$ from $M_{\rm HI}$. We combine $R_{\rm HI}$ with the median profile of $\Sigma_{\rm HI}$ as a function of $r/R_{\rm HI}$ to predict the profile of $\Sigma_{\rm HI}$ as a function of radius. We estimate the radial profile of $F_{\rm anchor}$ with the radial profiles of $\Sigma_{\rm HI}$ and Σ_{*} based on Equation (2). We compare the $F_{\rm anchor}$ profile with $P_{\rm ram}$ to determine the radial range where $F_{\rm anchor} < P_{\rm ram}$. We then accumulate the $\Sigma_{\rm HI}$ profile within that radial range to estimate the mass of strippable H I, and calculate $f_{\rm RPS,pred}$. These steps are also summarized in Figure 4. A similar technique was used in Wang et al. (2020a) to successfully predict the H I mass within and beyond the optical radius of individual galaxies. Comparing the directly calculated $f_{\rm RPS,pred}$ with $f_{\rm RPS}$ for the resolved-RPS candidates suggests a correction factor of 1.4 be multiplied to $f_{\rm RPS,pred}$ in order to match $f_{\rm RPS}$. We show in Figure 2(c) that $f_{\rm RPS,pred}$ is a good predictor of $f_{\rm RPS}$ for the resolved-RPS candidates, after such a correction. Thus, $f_{\rm RPS,pred}$ hereafter has all been corrected in this way. A maximum value of unity is set for $f_{\rm RPS,pred}$ after the correction.

The correcting factor is likely because the median profile misses the H I tails (lopsidedness) in the outer disks caused by RPS, and also misses the suppressed H I inner disks possibly as a result preprocessing (Hess & Wilcots 2013; Bahé & McCarthy 2015). Hints for these two features can be seen by comparing the H I radial profiles of the resolved galaxies to the median profile of late-type galaxies (Wang et al. 2016, 2020a) (Figure 2(b)). The deviation of shape in H I radial profiles cannot be fully explained as a result of beam smearing, as we find that the underestimation of $f_{\rm RPS}$ with $f_{\rm RPS,pred}$ does not increase with decreasing H I disk sizes. We caution that applying this correcting factor manually sets a minimum value of 0.15 dex for $f_{\rm RPS,pred}$, although it does not significantly affect our major conclusion, that for many of the r1-RPS candidates, the stripping efficiency is low. Note that such a treatment does not affect our identification of r1-RPS candidates, which were performed beforehand based on the size–mass relation of H I.

In the rest of the paper, we analyze the RPS and r1-RPS candidates separately. We use the r1-RPS sample for statistical trends, counts, and distributions in Sections 3 and 4, though we also display corresponding results of the RPS sample for a reference. We further use the resolved sample for a detailed analysis of the RPS history in Section 5, through comparing the galactic radial profiles of anchoring forces with the ram pressure levels at different $d_{\rm proj}$.

Table 1 lists the RPS properties of the galaxies derived above.

3. Distribution of Galaxies in the Projected Phase–Space Diagram

The main goal of this section is to obtain an overview of the distribution pattern of the H I -detected galaxies and r1-RPS candidates in the Hydra cluster and quantify the frequency of r1-RPS candidates among H I-detected galaxies. The projected phase–space diagram is a good tool for statistically separating virialized cluster members, infalling galaxies, and background/foreground galaxies (Oman & Hudson 2016). Previous studies found good correspondence between the projected phase–space diagram positions and H I richness of galaxies (Solanes et al. 2001; Jaffé et al. 2015; Yoon et al. 2017). An investigation of the projected phase–space diagram of optically detected galaxies in Hydra was presented by Lima-Dias et al. (2021).

The top panel of Figure 3 displays the distribution of WALLABY-detected galaxies in the projected phase–space diagram, in comparison to that of optically identified Hydra member galaxies from Kourkchi & Tully (2017). It shows that the H I-detected galaxies tend to avoid the inner part

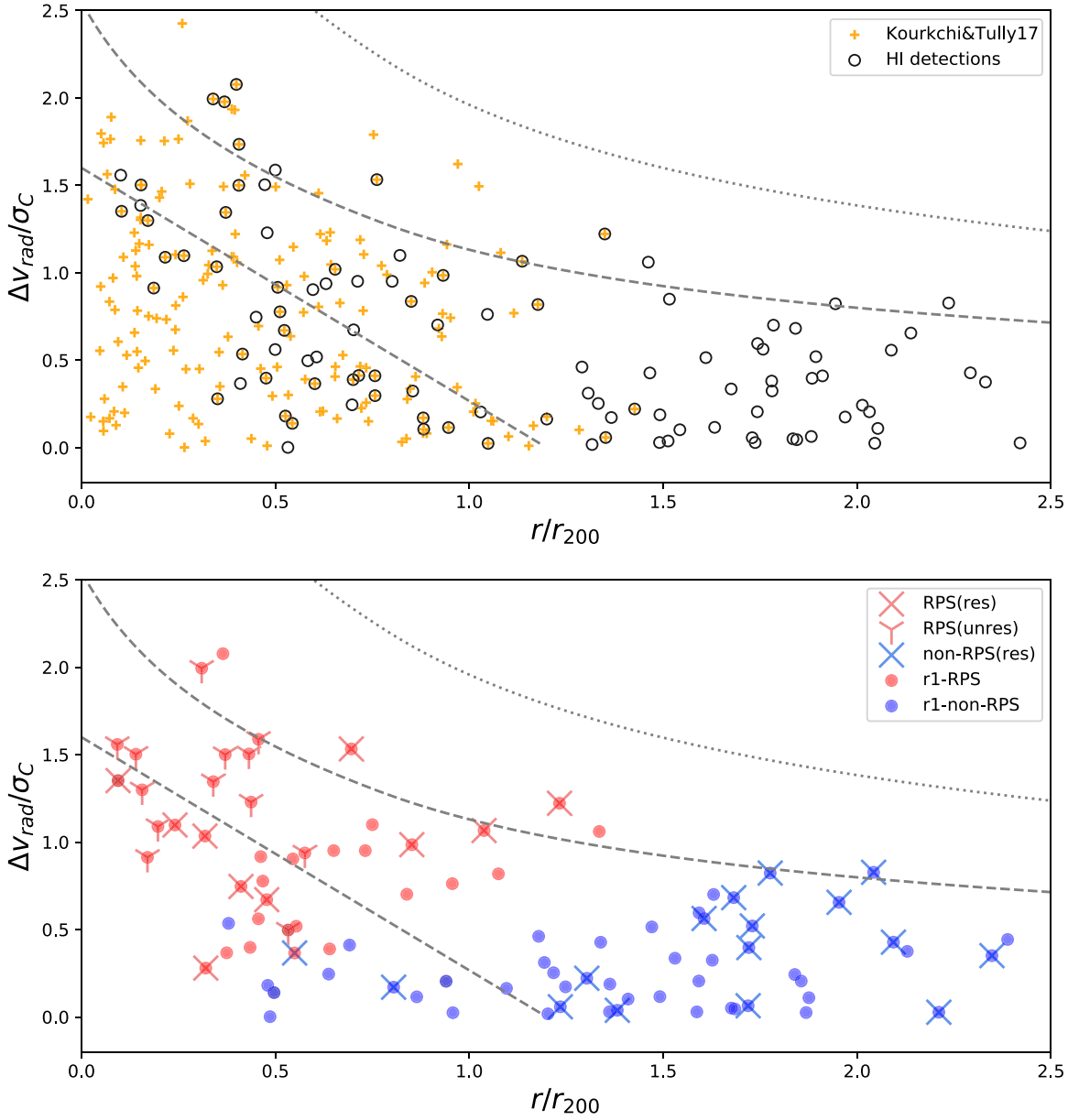

Figure 3. The projected phase–space diagram of the Hydra cluster. The dashed straight line marks the border of the virialized region, and the dashed (dotted) curve shows the averaged (upper limits of) projected escape velocities as a function of the projected cluster-centric distance $d_{\rm proj}$, which are expected for a Navarro–Frenk–White dark matter profile with a concentration of 4 (Navarro et al. 1997). Top: optical members of the Hydra cluster from Kourkchi & Tully (2017) in orange pluses and all the H I detections of WALLABY in black circles. Bottom: Only galaxies from the main sample are displayed. The resolved-RPS (non-RPS) candidates are marked by red (blue) crosses, respectively, and the unresolved RPS candidates in red *tri-down* symbols. The filled circles are colored red (blue) if they are in the r1-RPS (r1-non-RPS) type.

($d_{\rm proj} < 0.5r_{200}$) of the virialized region in the projected phase–space diagram, in contrast to the optical members of the cluster. It suggests that the recent infallers are more likely H I rich and is consistent with previous findings (Jaffé et al. 2015).

In the bottom panel of Figure 3, we compare the projected phase–space distributions of r1-RPS and r1-non-RPS candidates. The r1-RPS candidates tend to be within $1.25r_{200}$ and have higher $\Delta v_{\rm rad}$ than the other galaxies in the cluster, which is expected from the way that ram pressure strength is estimated (Gunn & Gott 1972), but the amount of H I and the anchoring force also play a role in the exact distribution of the galaxies in the projected phase–space diagram. Out to a $d_{\rm proj} \sim 1.25r_{200}$, 70% (44%) of the H I-detected galaxies in Hydra are r1-RPS (RPS) candidates.

4. H I Richness and the Influence from RPS

In this section, we present an overview of the H I richness of the detected galaxies and assess the extent of changes the current level of RPS will make to those H I masses ($M_{\rm HI}$).

Figure 5(a) presents the relation between $M_{\rm HI}$ and M_* for different subsamples. We can see that the $M_{\rm HI}$ at a given M_* is systematically lower than the mean relation of the galaxy population detected in the blind H I survey ALFALFA (Huang et al. 2012), but systematically higher than the median relation of the targeted survey of M_*-selected galaxies in xGASS (Catinella et al. 2018). The discrepancy between ALFALFA and WALLABY galaxies, which is more conspicuous at the high stellar mass end, is not majorly caused by the environment, but due to a volume effect. Although both

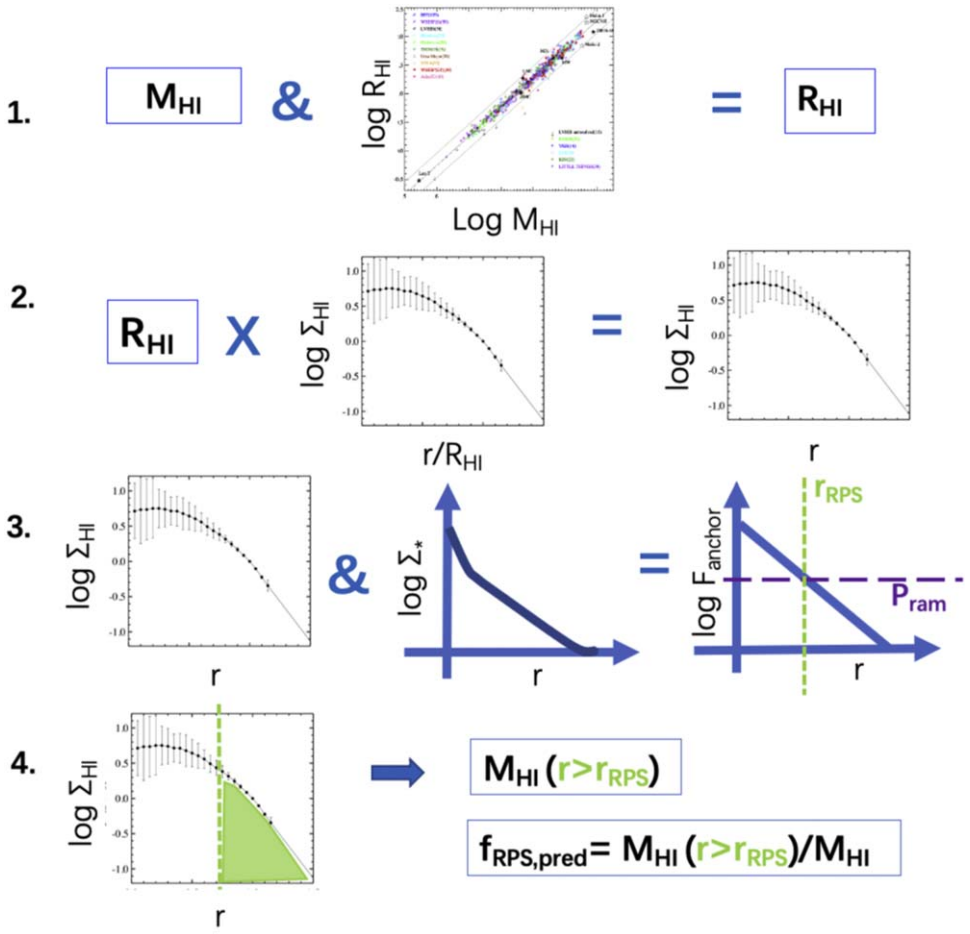

Figure 4. Procedure to estimate the fraction of strippable H I mass over the total H I mass ($f_{\rm RPS,pred}$). We use the H I size–mass relation H I ($R_{\rm HI}$ vs. $M_{\rm HI}$) and the median profile of H I surface density ($\Sigma_{\rm HI}$) as a function of $r/R_{\rm HI}$ from Wang et al. (2016). See text in Section 2.3.2 for details.

surveys are relatively shallow, approximately flux limited and have similar sensitivity, the WALLABY observations used here are limited to within ∼50 Mpc, whereas ALFALFA detections are within ∼200 Mpc (Haynes et al. 2011). At larger distances (where more massive systems are more likely found), the bias toward the most gas-rich systems becomes more important, and hence affects ALFALFA more strongly than this WALLABY volume. As the ALFALFA relation fully covers the M_* range of our sample, and roughly traces the upper envelope of $M_{\rm HI}$ distributions at a given M_* (also see Maddox et al. 2015), we will use it as a reference line to calculate the relative $M_{\rm HI}$ of galaxies at the present and after stripping the currently strippable H I (the post-RPS status). The discrepancy of $M_{\rm HI}$ from the xGASS relation indicates that the sample misses the gas poor, strongly depleted galaxies, due to the insufficient observational depth. Similarly, the $M_{\rm HI}$ distribution at a given M_* does not differ significantly from that of relatively isolated galaxies targeted by the Analysis of the interstellar Medium of Isolated GAlaxies (AMIGA) project (Verdes-Montenegro et al. 2005) either (not shown in Figure 5). So this study focuses on the onset and early stage of gas depletion in H I-rich galaxies.

The r1-RPS candidates have similar distributions of $M_{\rm HI}$ at a given M_* compared to the r1-non-RPS candidates, partly due to the relatively narrow range of $M_{\rm HI}$ detectable in WALLABY. There is a hint that the r1-RPS candidates lie on a slightly steeper $M_{\rm HI}$–M_* relation than the r1-non-RPS candidates, as indicated by the best-fit linear relations in Figure 5(b). The different slopes are mainly driven by the different $M_{\rm HI}$ distributions at low M_*. This supports the relatively greater effect of RPS on low-mass galaxies.

To understand the influence of the observed RPS on $M_{\rm HI}$, we investigate the distribution of $f_{\rm RPS,pred}$ in Figure 6(a). For 70% of the r1-RPS candidates, $f_{\rm RPS,pred}$ broadly falls below 0.9. We note that the 1σ scatter of the median relation of $M_{\rm HI}$ versus M_* from xGASS is ∼0.38 dex (Catinella et al. 2018), so the threshold $f_{\rm RPS,pred} = 0.9$ corresponds to a change in $M_{\rm HI}$ (i.e., $1 - f_{\rm RPS,pred}$) by around 2.5σ with respect to the median relation of $M_{\rm HI}$ versus M_*, after stripping the currently strippable H I. If we decrease the $f_{\rm RPS,pred}$ threshold to 0.8 (0.6), corresponding to a change in $M_{\rm HI}$ by 2 (1-)σ with respect to the median relation of $M_{\rm HI}$ versus M_*, then 68% (58%) of the r1-RPS candidates still have $f_{\rm RPS,pred}$ below the that. The large fraction of galaxies with low values of $f_{\rm RPS,pred}$ implies that the present RPS may not strongly deplete H I in many of the affected galaxies (partly a result of sample bias toward the H I-rich galaxies).

The parameter $f_{\rm RPS,pred}$ (and $f_{\rm RPS}$) relates to the amount of strippable H I, consisting of a spectrum of unresolved clouds with kinematics between those that are right to be accelerated by ram pressure and those that are right to disappear into the ICM. We investigate the post-RPS status quantified as $M_{\rm HI}(1 - f_{\rm RPS})$ and $M_{\rm HI}(1 - f_{\rm RPS,pred})$ for the RPS and r1-RPS candidates. For display purposes, we set the minimum post-RPS $M_{\rm HI}$ to be $10^{5.5}\,M_\odot$.

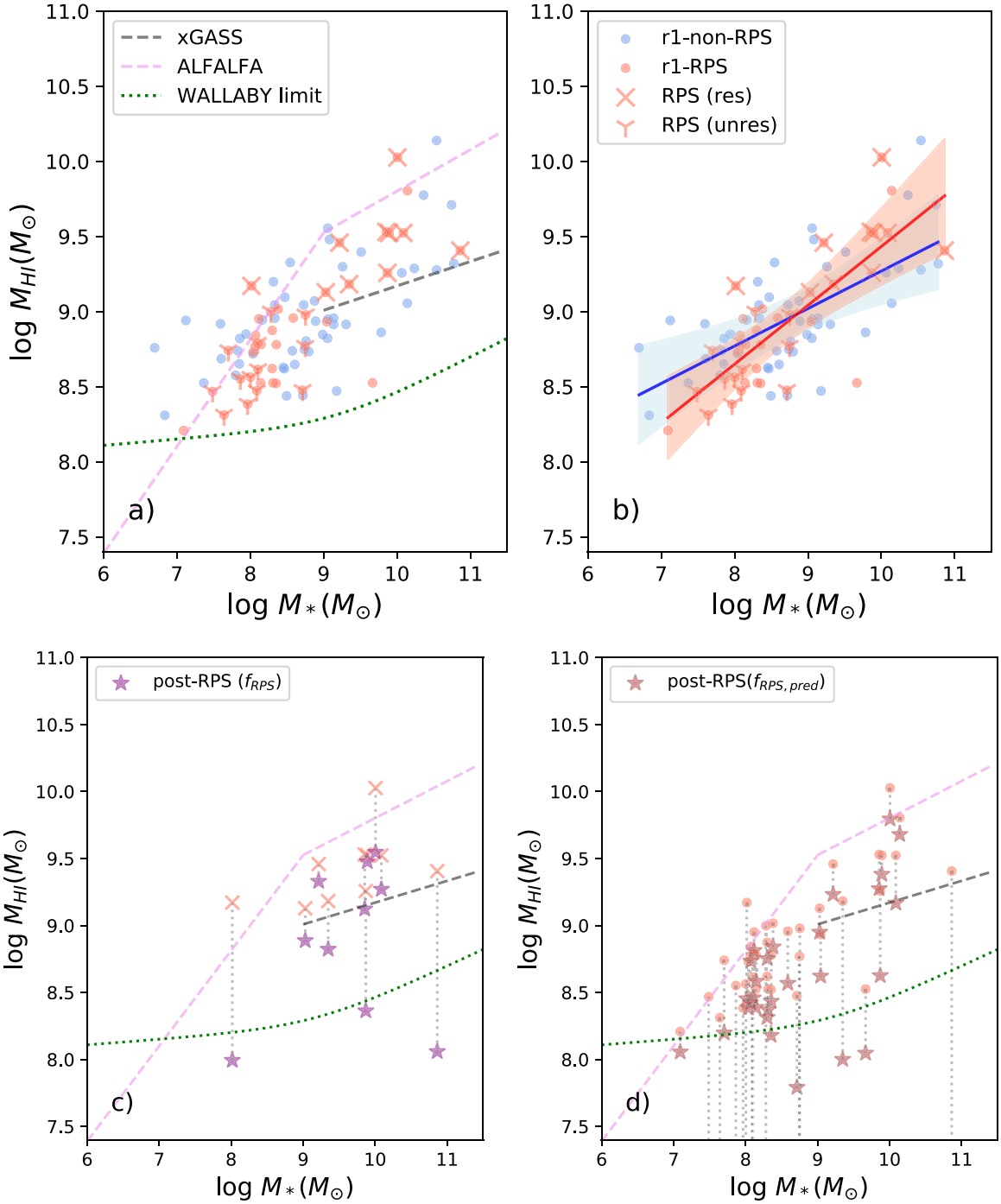

Figure 5. The relation between the H I mass ($M_{\rm HI}$) and the stellar mass (M_*) of the main sample. Panel (a): different types of galaxies are plotted in the same symbols as in the bottom panel of Figure 3. We mark the mean relations from xGASS (gray dashed line) and ALFALFA (pink dashed line), and the detection limit of WALLABY (green dotted line, see text). Panel (b): the best-fit linear relations for the r1-RPS (red) and r1-non-PRS (blue) populations. The shaded regions mark the 1σ uncertainty of fitting. Panel (c): brown stars plot the predicted position (post-RPS status) of galaxies after subtracting the strippable H I, i.e., $M_{\rm HI}(1-f_{\rm RPS})$ vs. M_*. Dotted lines link the observed and post-RPS positions of each galaxy. Panel (d): similar to panel (c), but with the post-RPS H I mass estimated with $f_{\rm RPS,pred}$ instead of $f_{\rm RPS}$. As indicated by the dotted lines, many post-RPS positions are at $M_{\rm HI}$ lower than the displayed range.

We compare the post-RPS $M_{\rm HI}$ at a given M_* with the detection limit of WALLABY in Figures 5(c) and (d). We estimate the WALLABY detection limit for H I flux,

$$f_{\rm lim}\,/({\rm Jy\ km\ s^{-1}}) = F_{\rm thresh} F_{\rm smooth}\,\sigma_{\rm cube}\,2v_{\rm rot}, \quad (3)$$

where the line width $v_{\rm rot}$ (km s^{-1}) is the rotational velocity predicted from the baryonic Tully–Fisher relation (McGaugh et al. 2000) assuming an edge-on view. The baryonic mass is the sum of M_* and 1.4 (to account for helium) times $M_{\rm HI}$ predicted from the mean relation of $M_{\rm HI}$ versus M_* taken from xGASS and extrapolated to the full M_* range. The factor $F_{\rm thresh} = 3.5$ is the threshold for flux detection in units of the cube rms $\sigma_{\rm cube} = 2$mJy beam^{-1}. The factor $F_{\rm smooth}$ is set to $1/7.75$, accounting for the maximum extent of smoothing in the channel maps (2 FWHM of Gaussian beams across), and in the velocity direction (15 channels) during the source finding. Our

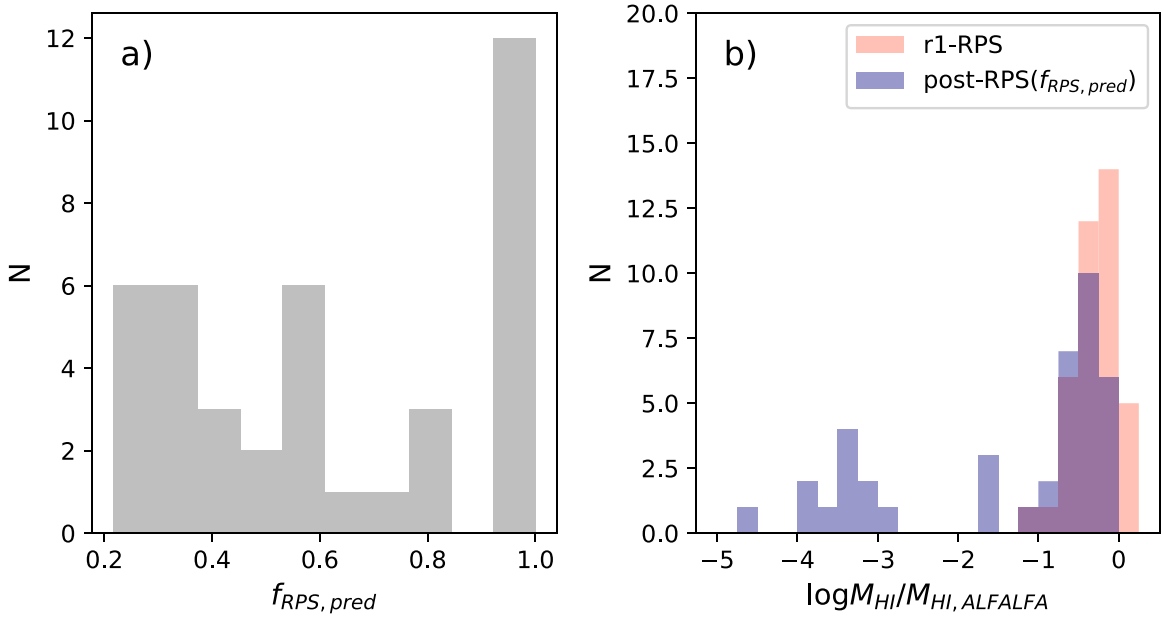

Figure 6. Distributions of the RPS strengths for the r1-RPS candidates. Panel (a) plots the predicted mass fraction of strippable H I ($f_{\rm RPS,pred}$). Panel (b) plots the difference of $M_{\rm HI}$ at a given M_* with respect to the ALFALFA mean relation of $M_{\rm HI}$ vs. M_* ($\log M_{\rm HI}/M_{\rm HI,ALFALFA}$). The distributions of $\log M_{\rm HI}/M_{\rm HI,ALFALFA}$ at the present and in the post-RPS status after removing the strippable H I (i.e., $M_{\rm HI}(1-f_{\rm RPS,pred})/M_{\rm HI,ALFALFA}$) are plotted in red and blue, respectively.

estimate for $f_{\rm lim}$ and $M_{\rm HI,lim}$ is only a rough approximation, for multiple smoothing kernels were used in the source finding by SoFiA, and SoFiA further exploits a reliability parameter to exclude unreliable threshold-based detections by comparing pixel distribution properties between the detected sources and pure noise (Serra et al. 2012, 2015). These steps are missing in our rough derivation of the detection limit and may be partly responsible for missing detections at high M_* ($>10^9\,M_\odot$) between the derived detection limit and the xGASS relation in Figure 5. Despite these complexities, the derived detection limit is close to the observed lower limit of detected fluxes at least for the low-M_* galaxies (Figure 5(a)) and is enough for the following analysis.

In Figures 5(c) and (d), we examine whether the post-RPS status of the r1-RPS (RPS) candidates will be observable by WALLABY in order to check the efficiency of RPS. It also helps assess whether it is feasible to study the early (relatively weak) stage of RPS based on the relatively shallow data of WALLABY. In other words, if all the post-RPS H I masses were below the WALLABY detection threshold, then RPS would be highly efficient in the Hydra cluster in depleting the total H I, and WALLABY would not be very useful to study even the early stage of RPS. Based on the analysis of $f_{\rm RPS}$ (Figure 5(c)), three out of the 10 resolved-RPS candidates will be undetected (below the WALLABY detection threshold) after the present stripping. Based on the analysis of $f_{\rm RPS,pred}$ (Figure 5(d)), 39% (23%) of the r1-RPS candidates with M_* below (above) $10^9\,M_\odot$ will be undetected after the present stripping, but more than half of the r1-RPS candidates will only drop slightly in $M_{\rm HI}$ after the present removal, indicating the instantaneous RPS to be weak in these galaxies.

In Figure 5(d), we also compare these post-RPS $M_{\rm HI}$ at a given M_* with the ALFALFA mean relation. From Figure 5(d), we can see that $M_{\rm HI}$ changes significantly (by >1 dex) for a few of the r1-RPS candidates, but by a relatively small extent (a few 0.1 dex) for the remaining many r1-RPS candidates. We calculate $M_{\rm HI}/M_{\rm HI,ALFALFA}$, the difference of $M_{\rm HI}$ from that indicated by the ALFALFA mean relation at the given M_*. Because many post-RPS $M_{\rm HI}$ drop below the displayed range in Figure 5(d), we show the distributions of $M_{\rm HI}/M_{\rm HI,ALFALFA}$ for the r1-RPS galaxies at the present and in the post-RPS status in Figure 6(b). By doing so, the fraction of r1-RPS galaxies undergoing big or small changes in $M_{\rm HI}$ after the present stripping can be better seen. We can see that, after stripping the currently strippable H I, most ($\sim 2/3$) of the r1-RPS candidates will remain relatively gas rich with $\log M_{\rm HI}/M_{\rm HI,ALFALFA} > -1$, and only $\sim 1/3$ of them will be severely depleted in H I. We investigated the positions of the $1/3$ most stripped galaxies in the projected phase–space diagram (not displayed in this paper). Not surprisingly, they tend to locate in the region with $\Delta v_{\rm rad}/\sigma_C > 1$ and $d_{\rm proj}/r_{200} < 0.5$, i.e., the region with the highest level of $P_{\rm ram}$.

The distribution of the post-RPS H I richness (with respect to the WALLABY detection limit and with respect to the ALFALFA relation) helps explain the similarity of $M_{\rm HI}$ at a given M_* between the r1-RPS and r1-non-RPS candidates. After a characteristic timescale for removing the currently strippable H I (the fraction indicated by $f_{\rm RPS,pred}$), the strongly stripped galaxies will drop below the detection limit of WALLABY, the weakly stripped galaxies will only have a slightly decreased $M_{\rm HI}$, and some currently r1-non-RPS candidates will become r1-RPS candidates and recharge the population of H I-rich r1-RPS population. In other words, the relatively narrow dynamical range of $M_{\rm HI}$ detectable by WALLABY, the cosmological context of galaxy infall, and the weak nature of a large fraction of the RPS events may have worked together to produce a $M_{\rm HI}$–M_* relation for the r1-RPS population that is very close to that of the r1-non-RPS population.

To summarize, comparing the post-RPS $M_{\rm HI}$ to the WALLABY detection limit and to the ALFALFA $M_{\rm HI}$–M_* relation both suggest that, the current strength of RPS can significantly deplete some galaxies (strong RPS, $f_{\rm RPS} > 0.9$), but only weakly

reduce $M_{\rm HI}$ (weak RPS, $f_{\rm RPS} < 0.9$) for a large fraction of the affected galaxies.

At a first glance, a single temporal snapshot may not look particularly meaningful as the ram pressure will change (usually becoming strong) as galaxies move through the cluster; also, it may look obvious that $f_{\rm RPS}$ should be low in many of these galaxies as they are not highly H I deficient. However, these results provide a first, comprehensive view of the weak ram-pressure regime in a nearby massive cluster, at a uniform detection limit. Although the instantaneous $f_{\rm RPS,pred}$ is low in many cases, the compound effect is significant as galaxies travel through a large distance (and over a long time, $\sim$2 Gyr if traveling radially with a velocity of σ_C) from where ram pressure starts to strip H I ($\sim$1.25 r_{200}), before reaching the core region ($<0.25r_{200}$, see Section 5.2, Figure 9) where H I is stripped throughout the disks. Such a cumulative effect has been hinted at in past hydrodynamic simulations, as the gas tails appear early (e.g., Tonnesen 2019) and are as prevalent in cluster galaxies as for the Hydra cluster (e.g., Yun et al. 2019) near the virial radius. Steinhauser et al. (2016) showed in their hydrodynamic simulations that at least for the low-mass galaxy model ($M_* = 8.25 \times 10^9\,M_\odot$), the curve of growth of the stripped gas mass as a function of time is quite shallow (in contrast to an abrupt increase) during the RPS history. Although the stripping of the outlying H I may not immediately affect the star-forming gas concentrated in the inner disk, it represents a shrinking of the gas reservoir for future star formation and preludes the final gas depletion and star formation quenching. In order to break the degeneracy of H I depleting effects from RPS, other environmental effects, and galactic internal mechanisms, it is necessary to consider the cumulative RPS effect. In the future, many similar cluster observations will be provided by WALLABY and combining them with cosmological simulations in a way like that of Rhee et al. (2020), Oman & Hudson (2016), and Oman et al. (2021) will eventually quantify the cumulative effects of weak RPS.

5. RPS of the Resolved Galaxies

The H I images of resolved galaxies provide us with the opportunity to investigate how RPS will deplete the H I in these galaxies. We note that these resolved galaxies typically (in 90%) have $M_{\rm HI} > 10^{9.1}\,M_\odot$ and $M_* > 10^{8.4}\,M_\odot$, so they represent a relatively restricted sample.

We investigate the capability of galaxies to restore their existing H I disks against ram pressure during the infall. We do a simplified experiment of putting each H I disk in our resolved sample at different projected distances d, and estimate the expected H I stripping fractions ($f_{\rm RPS}(d)$). In the remaining part of this section, all estimates as a function of d is denoted with "(d)", and the real galactic properties of the present are denoted with the subscript "now" to avoid confusion. For each galaxy, we estimate the expected radial velocity offset at d assuming the same infall acceleration profile as indicated by the projection averaged curve of v_{esc} as a function of $d_{\rm proj}$ (Figure 3),

$$\Delta v_{\rm rad}(d) = (\Delta v^2_{\rm rad,now} + (v^2_{\rm esc}(d) - v^2_{\rm esc,now}))^{0.5}. \quad (4)$$

We then estimate the ram pressure $P_{\rm ram}(d)$ at $v_{\rm rad}(d)$ using the ICM density at d. We compare $P_{\rm ram}(d)$ with the anchoring force profile of the galaxy, and calculate $f_{\rm RPS}(d)$.

We plot the curve of $f_{\rm RPS}(d)$ as a function of d for both resolved-RPS and non-RPS candidates in Figure 7. Each curve describes the effective ram pressure strength as a function of d, measured by the anchoring force of the current disk. We define d_x to be the projected cluster-centric distance where $f_{\rm RPS}(d) = x$ in the curve of a galaxy. So that $d_{0.1}$ indicates the maximum d where the present H I disk can start to be stripped. From Figure 7(b), there is quite a wide distribution of $d_{0.1}$ for the currently non-RPS candidates, ranging from 0.5–1.7r_{200}, with a median value of 1.1r_{200}. It is consistent with the wide $d_{\rm proj}$ range found for the r1-RPS candidates.

In the following, we will discuss questions related to the beginning and process of RPS based on these curves.

5.1. Time Needed to Strip the Currently Strippable H I in the RPS Candidates

For each of the resolved-RPS candidates, at a projected distance of $d_{0.1}$, which by definition is higher than $d_{\rm now}$, the ram pressure is already high enough to strip some of the currently strippable H I, but the strippable H I at $d_{0.1}$ can still be partly observed at the present because the strippable H I clouds do not immediately disappear into the ICM. The parameter $d_{0.1} - d_{\rm now}$ is an indicator ($\sim$upper limit) of the timescale ($\tau_{\rm RPS}$) needed for ram pressure to remove the strippable H I.

From Figure 7(a), $d_{0.1} - d_{\rm now} < 0.2r_{200}$ for all the resolved-RPS candidates, and also $<0.1r_{200}$ except for two galaxies (239 and 244 in Figure 10, with WALLABY ID J104059-270456 and J104142-284653, respectively). A distance of $0.1r_{200}$ takes $\sim$200 Myr for a galaxy with velocity σ_C to travel through, suggesting that RPS is a relatively fast mechanism (with a timescale of approximately hundreds of megayears) when removing the strippable gas.

We roughly estimate $\tau_{\rm RPS}$ for the resolved-RPS candidates by considering two scenarios. In the first scenario, the RPS is strong and the stripped H I cloud quickly reaches the escape velocity. The escape timescale is estimated as $\tau_{\rm esc} = \sqrt{2}\,v_{\rm rot}\,\Sigma_{{\rm HI},p50}/P_{\rm ram}$ (Vollmer et al. 2001), where $\Sigma_{{\rm HI},p50}$ is the median $\Sigma_{\rm HI}$ of the currently strippable H I. In the second scenario, the RPS is weak so that the stripped cloud is evaporated in the ICM after leaving the H I disk before being accelerated enough to escape. The timescale is the sum of the time needed for the cloud to rise a distance h above the disk and the time needed for the cloud to be evaporated. The former timescale is estimated as $\tau_{\rm rise} = (2h\Sigma_{{\rm HI},p50}/P_{\rm ram})^{0.5}$ (Vollmer et al. 2001), where we assume $h = 5$ kpc. According to Cowie & McKee (1977), the evaporating timescale is estimated as

$$\tau_{\rm evap} = \frac{9.07 \times 10^7 (N_{{\rm HI},p50}/10^{20}\,{\rm cm^{-2}})}{2.73 (n_{\rm ICM}/\,{\rm cm^{-3}})(T/K)^{0.5}\sigma_0^{3/8}}\ {\rm yr}$$
$$\sigma_0 = \frac{(T/1.54 \times 10^7\,K)^2}{(n_{\rm ICM}/{\rm cm^{-3}})(R_c/{\rm pc})}, \quad (5)$$

where $n_{\rm ICM}$ is the ICM density, $N_{{\rm HI},p50}$ is the column density corresponding to $\Sigma_{{\rm HI},p50}$, the Hydra ICM temperature $T = 3.76 \times 10^7\,K$ (Eckert et al. 2011), and as in Vollmer et al. (2001) we assume a cloud radius of $R_c = 10$ pc. Then, $\tau_{\rm RPS}$ is estimated as the lesser of $\tau_{\rm rise} + \tau_{\rm evap}$ and $\tau_{\rm esc}$. In the presence of magnetic fields, the real $\tau_{\rm evap}$ can be a few times longer, but ignoring this effect does not significantly affect our results because $\tau_{\rm rise} \gg \tau_{\rm evap}$ in all cases. We also ignored the gravitational force from the galaxy when estimating $\tau_{\rm esc}$ and $\tau_{\rm rise}$, but this uncertainty is mitigated by the fact that most of the ram pressure stripped pixels in the H I image have $P_{\rm ram} > 2F_{\rm anchor}$ (Figure 10). Nevertheless, these timescales should only be viewed as an

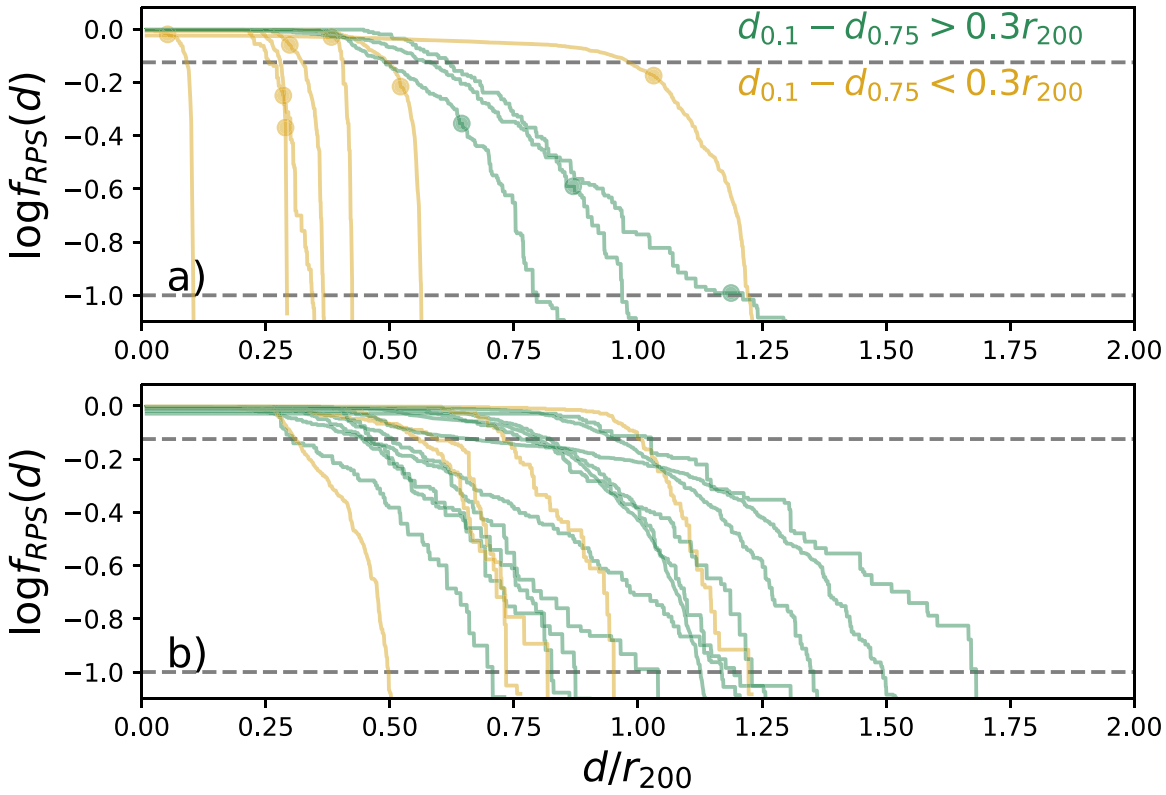

Figure 7. The relation between expected fraction of strippable H I ($f_{\rm RPS}(d)$) at different projected cluster-centric distances (d/r_{200}) for the resolved galaxies. The steep (shallow) curves, which take less than (at least) $0.2r_{200}$ for $f_{\rm RPS}(d)$ to increase from 0.1–0.75, are in orange (green). The horizontal dashed lines mark the positions for $f_{\rm RPS}(d)$ equaling 0.1 and 0.75. Panel (a): for the RPS candidates; their observed $d_{\rm proj}$ and $f_{\rm RPS}$ are marked as dots. Panel (b): for the non-RPS candidates; $d_{\rm proj}$ are larger than the displayed maximum d of each curve.

order-of-magnitude estimate, due to uncertainties from the disk inclination and other factors. From Figure 8, most of the ram pressure stripped gas is lost through evaporation in the RPS candidates, and the values of $\tau_{\rm RPS}$ are consistent with our interpretation of the $f_{\rm RPS}(d)$ curves of the resolved-RPS candidates. The values are also consistent with theoretical predictions in the literature (e.g., Abadi et al. 1999; Roediger & Brüggen 2006; Tonnesen 2019). They support the view that RPS is a relatively quick process when removing the strippable gas, even for cases where the ram pressure is low and thus $f_{\rm RPS}$ is low.

5.2. Time Needed to Strip the Existing H I Reservoir

Another noticeable feature from Figure 7 is that the curves of $f_{\rm RPS,exp}$ have distinct slopes. We use $d_{0.1} - d_{0.75} < (>) 0.3r_{200}$ as the criteria of selecting the steep (shallow) $d_{\rm proj,ex}$ curves. The parameter $d_{0.1} - d_{0.75}$ can be viewed as an indicator of the length of time needed to remove the majority of the existing H I reservoir in a galaxy with ram pressure. Although the existing H I mass is different from the initial H I mass upon infall, investigating the time needed to significantly deplete it is still meaningful, as most of the galaxies in our sample are still relatively H I rich. Removing 75% of the H I is equivalent to decreasing $M_{\rm HI}$ by 0.6 dex. A distance of $0.3r_{200}$ takes ~600 Myr for a galaxy with velocity σ_C to travel through. If we change the indicator $d_{0.1} - d_{0.75}$ to $d_{0.1} - d_{0.9}$, the related distance (traveling time) will increase, and more of the resolved galaxies will be classified with shallow curves, but the conclusions are similar.

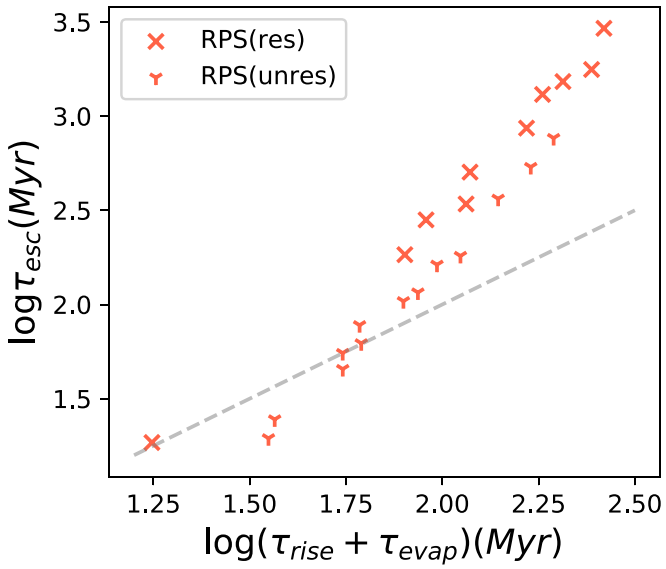

Figure 8. The estimated timescales for ram pressure stripped clouds to escape ($\tau_{\rm esc}$) and to be evaporated ($\tau_{\rm rise} + \tau_{\rm evap}$). The resolved (unresolved) RPS candidates are plotted in red crosses (down-tri shapes). The dashed line marks the position of $\tau_{\rm esc} = \tau_{\rm rise} + \tau_{\rm evap}$.

Galaxies with shallow $f_{\rm RPS}(d)$ curves tend to be stripped for a relatively long period of time (≥600 Myr, if we assume galaxies radially travel with an average speed of σ_C). Figure 7 suggests that, the resolved galaxies on shallow curves tend to have larger d than those on steep curves, with a Kolmogorov–

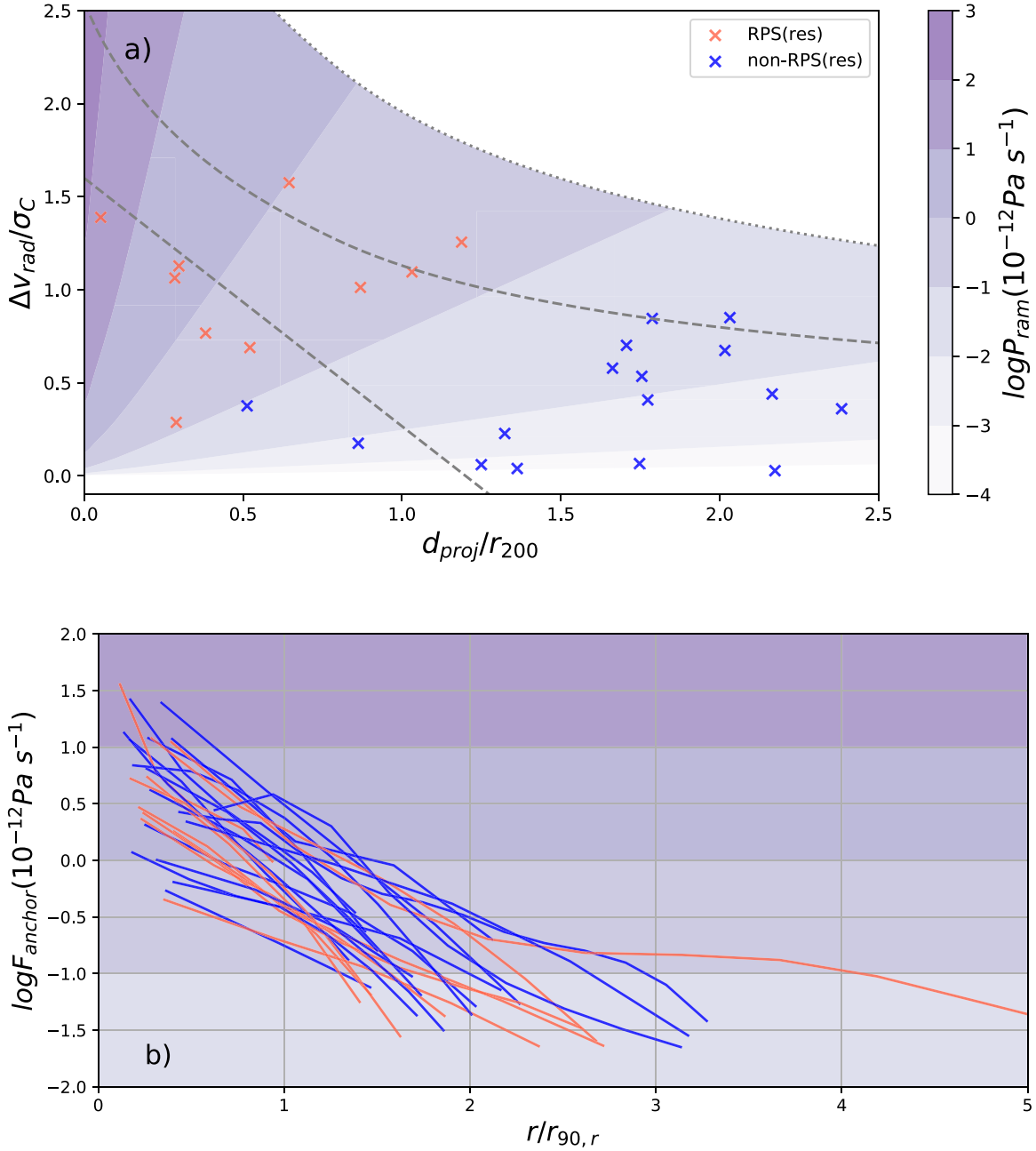

Figure 9. The ram pressure level of the Hydra cluster and the anchoring force profiles of all the resolved galaxies. Panel (a): the distribution of ram pressure ($P_{\rm ram}$) in the projected phase–space diagram. The projected phase–space diagram is the same as in Figure 3. The resolved-RPS and non-RPS candidates are in red and blue crosses, respectively. Panel (b): the azimuthally averaged anchoring force ($F_{\rm anchor}$) radial profile of galaxies. The resolved-RPS and non-RPS candidates are in red and blue, respectively. The radii of each profile are normalized by the 90% light radius of the galaxy in the r band ($r_{90,r}$). The largest radius for each galaxy is determined by the size of the H I disk. The space of $F_{\rm anchor}$ is color coded with the same scales as $P_{\rm ram}$ in panel (a).

Smirnov test probability of 0.01 for the distributions of $d_{\rm proj}$ to be similar among the two subsamples. Due to the relatively small sample size, we do not find statistically significant differences in other properties between the galaxies with shallow and steep $f_{\rm RPS}(d)$ curves. Figure 7(b) suggests that most (∼70%) of the currently non-RPS candidates will start the RPS process with shallow $f_{\rm RPS}(d)$ curves.

The shallow $f_{\rm RPS}(d)$ profiles, particularly for the non-RPS candidates in the future, are likely due to the shallow ICM density profile beyond the core region of the cluster and the extended nature of H I disks. Figure 9 demonstrates these two effects. In Figure 9(a), $\log P_{\rm ram}$ rises by three orders of magnitude when $d_{\rm proj} < 0.5r_{200}$ and only rises by two orders of magnitude when $2.5r_{200} > d_{\rm proj} > 0.5r_{200}$. In Figure 9(b), the radial range of $F_{\rm anchor}$ profiles (H I disks) extends far beyond the optical disk ($r_{90,r}$) in many galaxies, and the profiles rise relatively smoothly (roughly exponentially) toward the galaxy centers. In these resolved galaxies, $F_{\rm anchor} > 10^{-13}$ Pa s^{-1} throughout most of the radial ranges. A ram pressure of 10^{-13} Pa s^{-1} already starts at $d_{\rm proj} \sim 1.25r_{200}$ in the infall region (far beyond the triangle of virialized region) of the projected phase–space diagram (Figure 9(a)), consistent with where RPS and r1-RPS candidates start to be detected. On the other hand, $P_{\rm ram}$ needs to rise above 10^{-12} Pa s^{-1} (the typical $F_{\rm anchor}$ at $r_{90,r}$) in order to effectively strip the H I within the optical disks. This requires the infalling galaxies to reach $d_{\rm proj} < 0.5r_{200}$. It needs to further rise above

10^{-11} Pa s^{-1} in order to completely strip the H I from the majority of those resolved galaxies, which requires the infalling galaxies to reach $d_{\rm proj} < 0.25r_{200}$. Indeed very few galaxies (in total four) are detected by WALLABY in the triangular region (the *stripping zone* defined in Jaffé et al. 2015) of the projected phase–space diagram where $P_{\rm ram} > 10^{-11}$ Pa s^{-1}. The key point to make here is that, galaxies travel for a large $d_{\rm proj}$ (hence time) between the onset and end of RPS, emphasizing the importance of the effect of weak but cumulative RPS forces.

Thus, we have observed diversities in RPS not only for the instantaneous strength ($f_{\rm RPS}$), but also for the averaged speed ($d_{0.1} - d_{0.75}$). For the non-RPS candidates, there is further a diversity in $d_{\rm proj}$ for RPS to onset. Modern hydrodynamic simulations under a cosmological context predicted that most galaxies lose the majority of H I through RPS in one passage of infall into massive clusters, but there is a large scatter in the speed of H I depletion (Jung et al. 2018; Lotz et al. 2019; Oman et al. 2021), not only because of scatter in the infall orbits, but also because of scatter in the initial conditions. Our results are qualitatively consistent with the latter. The early, strong and rapid RPS associated with large $d_{0.1}$, high $f_{\rm RPS}$, and low $d_{0.1} - d_{0.75}$ is more likely to link with a fast depletion, while late, weak and slow RPS associated with small $d_{0.1}$, low $f_{\rm RPS}$, and high $d_{0.1} - d_{0.75}$ is more likely to link with a slow depletion. A closer comparison in distributions of $f_{\rm RPS}$ and $d_{0.1} - d_{0.75}$ between the observed and simulated data sets may help advance our understanding of the role of RPS in galaxy evolution, particularly when more clusters are observed in the future.

The diversity in RPS strength/speed may further link to the diversity in star-forming histories of cluster galaxies. There has been a debate in the observational literature regarding the time needed to quench the SFR of galaxies infalling into clusters. Analysis of star-forming histories has suggested a slow mode (2–4 Gyr; Rasmussen et al. 2012; Wetzel et al. 2013; Paccagnella et al. 2016) a fast mode (<1 Gyr; Muzzin et al. 2014; Boselli et al. 2016), and a combination of the two modes (Haines et al. 2013, 2015; Maier et al. 2019). In those studies, slow quenching was typically attributed to the effect of starvation where galaxies lose their hot gas halos due to RPS, stop gas accretion, and gradually quench when the remaining cold gas is consumed (Larson et al. 1980). Fast quenching was typically linked to strong RPS that effectively removes H I throughout the disks (Jaffé et al. 2015). Our results suggest that ram pressure starts to remove H I long before it affects the whole H I disk. Although there can be considerable delay between the significant removal of H I and the final quenching of star formation (Cortese & Hughes 2009; Boselli et al. 2014; Oman et al. 2021), the scatter in the timescale for RPS to deplete most of the H I in a disk may contribute to the scatter in the quenching timescale. The effect of weak RPS of H I on star formation is close to the traditionally defined starvation caused by the removal of the hot gas halo (Larson et al. 1980) because it gradually shrinks the extended H I disks, which serve as the reservoir instead of the direct material for star formation. The extended H I gradually flows radially inward (Schmidt et al. 2016) to fuel the inner disks, and the inner H I is converted to the molecular gas and then stars (Bigiel et al. 2008; Wang et al. 2020a). But stripping of the H I should be more efficient than starvation in quenching, as H I is a closer step to star formation than the hot gas halo. The weak RPS of H I thus adds an intermediate step between the gentle starvation that starts at a large cluster-centric radii ($\sim 3r_{200}$, Bahé & McCarthy 2015) and the violent strong RPS prevalent near the cores of clusters ($<0.3r_{200}$, Jaffé et al. 2015), possibly leading to a stronger environmental effect and less room for galactic internal mechanisms (like stellar feedback) in interpreting the distribution of $M_{\rm HI}$ and SFR in cluster galaxies.

5.3. Caveats

Because the estimates of RPS strength suffer from uncertainties of projection, orbits, and other effects, the analysis above should be interpreted in a statistical sense, instead of a case-by-case manner. When interpreting our results, we ignore many physical processes, including the cooling of ionized gas, the falling back of the stripped H I, the depletion due to star formation and feedback, the redistribution of H I within the disk, the change in orbital directions, and external gravitational effects. Also, the analysis is not about removing all the H I from the initial conditions upon infall, but about removing what is left at the current epoch. Thus, the analysis should be viewed as qualitative, with order-of-magnitude estimates.

Quantifying the star-forming history (as in Boselli et al. 2016), using dynamic simulations combined with H I richness and star-forming history to constrain the infall orbits (Vollmer et al. 2001) and/or directly comparing the snapshots of RPS presented in this paper with cosmological hydrodynamic simulations in the future may assist in gaining further insight into the gas depletion and star formation quenching processes in clusters.

6. Summary

With the WALLABY observations, we for the first time map the H I in the Hydra cluster out to $2.5r_{200}$ (and full coverage out to $2r_{200}$), detecting 105 members or infalling galaxies and resolving 27 of them. We quantify the extent of H I RPS based on the H I images for the resolved galaxies and also based on predicted H I radial distributions for all the galaxies. We emphasize that the analysis is limited to the H I-rich galaxies that are at a relatively early stage of being processed by the cluster environment. Our main results are summarized below.

1. A large fraction of H I-rich galaxies in and near the Hydra cluster are affected by RPS. Within a projected distance of $1.25r_{200}$, over two-thirds of H I-detected galaxies are likely affected by RPS (the r1-RPS population).
2. A large fraction of the ram pressure affected galaxies are likely being weakly stripped at the current time. With the present level of ram pressure, $M_{\rm HI}$ in around one-third of the r1-RPS candidates may significantly drop (by >1 dex), but for the remaining two-thirds, $M_{\rm HI}$ only slightly changes (by a few 0.1 dex). The cumulative effects of weak RPS processes need to be further investigated.
3. At least for the resolved galaxies ($M_{\rm HI} > 10^{9.1}\,M_{\odot}$ and $M_{*} > 10^{8.4}\,M_{\odot}$) once onset, RPS is likely a slow process ($\gtrsim$600 Myr) for depleting the existing reservoir of H I in the galaxies. This is because for the H I-rich galaxies with extended H I disks, RPS can start at a relatively large cluster-centric distance ($d_{\rm proj} \sim 1.25r_{200}$, see Reynolds et al. 2021 for a detailed analysis for one such galaxy), where the ram pressure changes slowly with cluster-centric distance. The different $d_{\rm proj}$ for RPS to onset and the different speeds at which $f_{\rm RPS}$ rises as a function of $d_{\rm proj}$ may partly explain the scatter of quenching speed

found for the SFR of cluster galaxies in the literature (Wetzel et al. 2013; Haines et al. 2015; Boselli et al. 2016).

4. For most of the resolved-RPS candidates, stripping the strippable H I is likely a relatively quick process, on timescales of $\lesssim$200 Myr, consistent with theoretical predictions. This short timescale is supported by the short distance between the current $d_{\rm proj}$ and the predicted larger $d_{\rm proj}$ where part (10%) of the current H I disk could already be stripped. It is also supported by the rough estimates of $\tau_{\rm RPS}$ based on the cluster and galaxy properties, and simple kinematical and thermal models.

We look forward to expanding our analysis with larger samples from future WALLABY observations, supported by hydrodynamic and semi-analytical simulations.

We thank R. White, J. Fu, J.-Y. Tang, Z.-L. Zhang, L. Cortese, K. Oman, A. Stevens, and A. Bosma for useful discussions. J.W. acknowledges support from the National Science Foundation of China (12073002, 11721303). Parts of this research were supported by High-performance Computing Platform of Peking University. Parts of this research were conducted by the Australian Research Council Centre of Excellence for All Sky Astrophysics in 3 Dimensions (ASTRO 3D), through project number CE170100013. This project has received funding from the European Research Council (ERC) under the European Union's Horizon 2020 research and innovation program (grant agreement No. 679627; project name FORNAX). F.B. acknowledges funding from the ERC under the European Union's Horizon 2020 research and innovation program (grant agreement No.726384/Empire). L.V.M. acknowledges financial support from grants AYA2015-65973-C3-1-R and RTI2018-096228-B-C31 (MINECO/FEDER, UE), as well as from the State Agency for Research of the Spanish MCIU through the "Center of Excellence Severo Ochoa" award to the Instituto de Astrofísica de Andalucía (SEV-2017-0709). S.H.O. acknowledges support from the National Research Foundation of Korea (NRF) grant funded by the Korea government (Ministry of Science and ICT: MSIT) (No. NRF-2020R1A2C1008706).

The Australian SKA Pathfinder is part of the Australia Telescope National Facility, which is managed by CSIRO. Operation of ASKAP is funded by the Australian Government with support from the National Collaborative Research Infrastructure Strategy. ASKAP uses the resources of the Pawsey Supercomputing Centre. Establishment of ASKAP, the Murchison Radio-astronomy Observatory and the Pawsey Supercomputing Centre are initiatives of the Australian Government, with support from the Government of Western Australia and the Science and Industry Endowment Fund. We acknowledge the Wajarri Yamatji people as the traditional owners of the Observatory sites.

The Pan-STARRS1 Surveys (PS1) and the PS1 public science archive have been made possible through contributions by the Institute for Astronomy, the University of Hawaii, the Pan-STARRS Project Office, the Max-Planck Society and its participating institutes, the Max Planck Institute for Astronomy, Heidelberg and the Max Planck Institute for Extraterrestrial Physics, Garching, The Johns Hopkins University, Durham University, the University of Edinburgh, the Queen's University Belfast, the Harvard-Smithsonian Center for Astrophysics, the Las Cumbres Observatory Global Telescope Network Incorporated, the National Central University of Taiwan, the Space Telescope Science Institute, the National Aeronautics and Space Administration under grant No. NNX08AR22G issued through the Planetary Science Division of the NASA Science Mission Directorate, the National Science Foundation grant No. AST-1238877, the University of Maryland, Eötvös Loránd University (ELTE), the Los Alamos National Laboratory, and the Gordon and Betty Moore Foundation.

Appendix
Atlas and Table, and Additional Information on Individual Resolved-RPS Candidates

We show an atlas of the H I contours on the resolved-RPS candidates (Figure 10). We also list the galactic properties used in this study in Table 1.

The strongest, resolved-RPS candidate, NGC 3312, (189 in Figure 10, WALLABY ID: J103702-273359) was previously identified by its peculiar H I and blue light distributions (Gallagher 1978; McMahon et al. 1990, but see McMahon et al. 1992). Its neighbor, NGC 3314A also shows H I tails (McMahon et al. 1990), but overlaps with another bright galaxy NGC 3314B, so has been excluded from our analysis. A detailed analysis is under way for this system (K. M. Hess et al. 2021, in preparation).

One RPS candidate, ESO 501-G065 (212 in Figure 10, WALLABY ID: J103833-274357) shows a hint of a tidal tail in the optical with a corresponding H I tail. It may be a case similar to the Magellanic system where gravitational effects (tidal interactions or harassment) first perturb the galaxy and then ram pressure is able to override the anchoring force in the low density gas produced by the gravitational perturbation. We do not exclude this galaxy as it does not appear to experience a major merger. We leave a statistical study of the combined effects of ram pressure and tidal interactions in clusters to the future.

Detailed analysis of RPS in ESO 501-G075 (239 in Figure 10, WALLABY ID: J103655-265412) can be found in Reynolds et al. (2021).

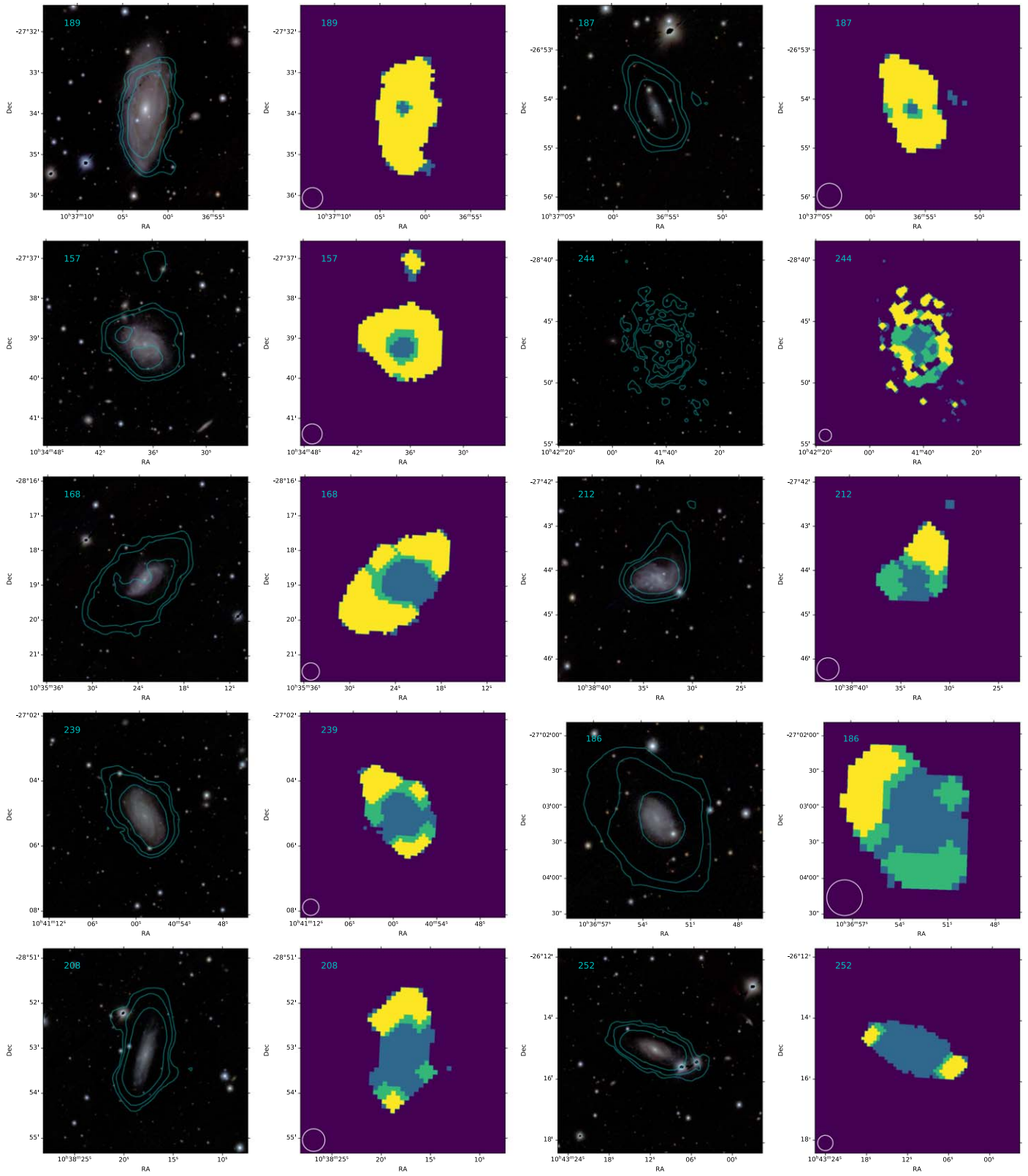

Figure 10. Atlas of resolved-RPS candidates. The galaxies are ordered by decreasing fraction of strippable H I, $f_{\rm RPS}$. Each galaxy has a pair of panels: the H I contours overlaid on the Pan-STARRS optical image and the RPS map. In the contour map, the cyan contours mark H I column density levels of 1, 2, and 5 times 10^{20} cm^{-2}. In the RPS map, the yellow and green colors mark the RPS pixels, which have $P_{\rm ram} > F_{\rm anchor}$, and the yellow pixels are those with $P_{\rm ram} > 2F_{\rm anchor}$. The blue color marks the ram pressure unaffected pixels. The white circle in the bottom-left corner of each RPS map shows the FWHM of the synthesis beam.

Table 1
Galaxy Properties

ID (1)	WALLABY ID (2)	$d_{\rm proj}/r_{200}$ (3)	$\Delta v_{\rm rad}/\sigma_C$ (4)	$\log M_*/M_\odot$ (5)	$\log M_{\rm HI}/M_\odot$ (6)	$\rm flag_{r1-RPS}$ (7)	$\rm flag_{RPS}$ (8)	$f_{\rm RPS,pred}$ (9)	$f_{\rm RPS}$ (10)
83	J102107-281054	2.16	0.44	8.5	9.1	0	0	⋯	⋯
97	J102411-285533	1.91	0.25	8.9	8.9	0	0	⋯	⋯
102	J102430-290904	1.94	0.03	8.4	8.6	0	0	⋯	⋯
103	J102439-244547	2.38	−0.36	8.3	9.0	0	0	⋯	⋯
104	J102439-274841	1.66	−0.21	6.7	8.8	0	0	⋯	⋯
116	J102621-291150	1.74	−0.05	8.2	8.9	0	0	⋯	⋯
117	J102629-285851	1.66	−0.03	7.8	8.6	0	0	⋯	⋯
118	J102636-245116	2.16	0.39	8.6	8.7	0	0	⋯	⋯
125	J102818-255446	1.52	0.12	6.8	8.3	0	0	⋯	⋯
127	J102911-302031	2.02	0.67	10.1	9.3	0	0	⋯	⋯
129	J102934-261937	1.23	0.32	8.7	8.7	0	0	⋯	⋯
130	J103002-284116	1.16	0.17	8.6	8.6	0	0	⋯	⋯
131	J103004-253630	1.49	−0.53	7.4	8.5	0	0	⋯	⋯
134	J103114-295837	1.69	0.72	8.5	8.6	0	0	⋯	⋯
135	J103124-295706	1.66	0.58	9.1	9.5	0	0	⋯	⋯
137	J103139-273049	0.69	−0.25	7.9	8.7	0	0	⋯	⋯
141	J103241-273137	0.55	0.14	9.2	8.5	0	0	⋯	⋯
142	J103244-283639	0.86	−0.17	10.5	9.3	0	0	⋯	⋯
143	J103248-273119	0.53	−0.19	9.1	9.0	0	0	⋯	⋯
144	J103250-301601	1.77	−0.41	10.2	9.3	0	0	⋯	⋯
146	J103258-274013	0.52	−0.94	8.6	9.0	1	0	0.59	⋯
147	J103259-273237	0.51	1.63	8.7	8.5	1	1	0.79	⋯
149	J103335-272717	0.43	−0.55	10.8	9.3	0	0	⋯	⋯
151	J103353-274945	0.43	−1.54	8.8	9.0	1	1	1.00	⋯
155	J103420-264728	0.56	0.93	8.4	8.5	1	0	0.54	⋯
156	J103420-265408	0.50	−0.00	7.9	8.8	0	0	⋯	⋯
157	J103436-273900	0.30	−1.13	9.9	9.3	1	1	0.77	0.87
160	J103455-273816	0.25	−1.12	7.5	8.5	1	1	1.00	⋯
161	J103459-280440	0.42	−2.13	9.7	8.5	1	0	0.67	⋯
162	J103502-293019	1.25	0.02	9.1	8.8	0	0	⋯	⋯
163	J103507-275923	0.36	−2.05	8.7	8.8	1	1	1.00	⋯
165	J103521-272324	0.20	−0.94	7.9	8.6	1	1	1.00	⋯
166	J103521-274137	0.21	−1.33	8.3	9.0	1	1	1.00	⋯
168	J103523-281855	0.52	−0.69	9.9	9.5	1	1	0.44	0.61
172	J103546-273840	0.15	1.60	8.1	8.8	1	1	1.00	⋯
174	J103602-261141	0.82	−0.72	8.1	8.5	1	0	0.27	⋯
176	J103603-245430	1.62	0.33	7.1	8.9	0	0	⋯	⋯
178	J103621-252235	1.32	0.44	9.3	8.9	0	0	⋯	⋯
179	J103627-255957	0.94	−0.78	7.1	8.2	1	0	0.30	⋯
180	J103644-251543	1.39	−0.11	8.8	8.8	0	0	⋯	⋯
181	J103645-281010	0.40	−0.38	8.4	9.0	1	0	0.34	⋯
182	J103646-293253	1.25	−0.26	8.7	9.0	0	0	⋯	⋯
183	J103650-260923	0.84	−0.12	8.9	9.1	0	0	⋯	⋯
186	J103653-270311	0.29	−0.29	9.0	9.1	1	1	0.34	0.43
187	J103655-265412	0.38	−0.77	8.0	9.2	1	1	0.81	0.93
189	J103702-273359	0.05	−1.39	10.9	9.4	1	1	1.00	0.96
190	J103704-252038	1.34	−0.03	9.1	8.9	0	0	⋯	⋯
192	J103719-281408	0.45	−0.41	8.3	8.5	1	0	0.30	⋯
194	J103722-273235	0.09	−1.54	8.0	8.6	1	1	1.00	⋯
195	J103725-251916	1.36	−0.04	10.5	10.1	0	0	⋯	⋯
200	J103738-281216	0.44	1.54	8.1	8.5	1	1	1.00	⋯
203	J103804-284333	0.77	1.13	8.4	8.8	1	0	0.55	⋯
204	J103805-250537	1.51	0.35	9.0	8.8	0	0	⋯	⋯
205	J103809-260453	0.91	−0.21	8.7	8.4	0	0	⋯	⋯
207	J103812-275607	0.33	−1.38	7.6	8.3	1	1	1.00	⋯
208	J103818-285307	0.87	1.01	9.2	9.5	1	1	0.41	0.26
210	J103821-254126	1.15	−0.47	8.0	8.7	0	0	⋯	⋯
211	J103828-283056	0.66	0.98	8.1	8.8	1	0	0.55	⋯
212	J103833-274357	0.29	1.06	9.3	9.2	1	1	0.93	0.56
213	J103840-283405	0.70	−0.42	9.8	8.9	0	0	⋯	⋯
214	J103841-253530	1.22	0.18	7.6	8.9	0	0	⋯	⋯
215	J103842-281535	0.53	−0.51	8.1	8.6	1	1	0.30	⋯
220	J103902-291255	1.09	−0.84	8.3	8.9	1	0	0.24	⋯

Table 1
(Continued)

ID (1)	WALLABY ID (2)	$d_{\rm proj}/r_{200}$ (3)	$\Delta v_{\rm rad}/\sigma_C$ (4)	$\log M_*/M_\odot$ (5)	$\log M_{\rm HI}/M_\odot$ (6)	flag$_{r1-{\rm RPS}}$ (7)	flag$_{\rm RPS}$ (8)	$f_{\rm RPS,pred}$ (9)	$f_{\rm RPS}$ (10)
222	J103914-271511	0.38	1.26	8.0	8.4	1	1	1.00	⋯
223	J103915-301757	1.75	0.07	10.4	9.8	0	0	⋯	⋯
225	J103922-293505	1.32	0.23	9.3	9.3	0	0	⋯	⋯
226	J103924-275442	0.44	−0.80	9.0	8.9	1	0	0.51	⋯
228	J103927-271653	0.40	−0.58	8.3	8.6	1	0	0.51	⋯
229	J103939-280552	0.54	−0.53	8.1	8.8	1	0	0.37	⋯
231	J103958-301130	1.71	−0.70	10.1	9.1	0	0	⋯	⋯
232	J104000-292445	1.25	0.06	8.3	9.2	0	0	⋯	⋯
233	J104004-301606	1.75	−0.53	9.5	9.4	0	0	⋯	⋯
234	J104016-274630	0.51	0.38	10.1	9.8	1	0	0.25	⋯
235	J104026-274853	0.54	0.96	7.7	8.7	1	1	0.71	⋯
236	J104048-244003	1.85	−0.11	8.3	9.0	0	0	⋯	⋯
238	J104058-274546	0.60	0.40	8.1	8.8	1	0	0.22	⋯
239	J104059-270456	0.64	1.57	10.1	9.5	1	1	0.56	0.44
240	J104100-284430	0.95	0.03	9.1	8.9	0	0	⋯	⋯
242	J104139-254049	1.32	0.19	7.8	8.7	0	0	⋯	⋯
243	J104139-274639	0.69	0.98	8.0	8.7	1	0	0.55	⋯
244	J104142-284653	1.03	1.10	10.0	10.0	1	1	0.41	0.67
246	J104221-291748	1.34	1.09	8.1	9.0	1	0	0.27	⋯
251	J104309-300301	1.79	−0.85	9.1	9.6	0	0	⋯	⋯
252	J104311-261500	1.19	1.26	9.9	9.5	1	1	0.28	0.10
253	J104326-251857	1.65	0.05	8.8	8.7	0	0	⋯	⋯
256	J104359-293304	1.59	−0.61	8.5	8.4	0	0	⋯	⋯
266	J104629-253308	1.82	−0.21	7.9	8.8	0	0	⋯	⋯
269	J104824-250944	2.17	0.03	10.7	9.7	0	0	⋯	⋯
270	J104905-292232	2.03	0.85	8.5	9.3	0	0	⋯	⋯
272	J105227-291155	2.37	−0.46	7.6	8.7	0	0	⋯	⋯

Note. Column (1): ID. Column (2): WALLABY identifier. Column (3): the cluster-centric projected distance. Column (4): the velocity distance from cluster center. Column (5): stellar mass. Column (6): H I mass. Column (7): flag for identification of r1-RPS candidates (the major sample studied in Sections 3 and 4), 1 for True and 0 for False. Column (8): flag for identification of RPS candidates (both resolved and unresolved), 1 for True and 0 for False. The identification of unresolved RPS candidates is incomplete. Column (9): the fraction of H I mass under RPS derived from predicted H I radial profiles. Column (10): the fraction H I mass under RPS derived from H I moment-0 maps for the resolved-RPS candidates.

ORCID iDs

Jing Wang (王菁) https://orcid.org/0000-0002-6593-8820
Lister Staveley-Smith https://orcid.org/0000-0002-8057-0294
Barbara Catinella https://orcid.org/0000-0002-7625-562X
Li Shao (邵立) https://orcid.org/0000-0003-2015-777X
T. N. Reynolds https://orcid.org/0000-0002-6606-5953
Bumhyun Lee https://orcid.org/0000-0002-3810-1806
Shun Wang (王舜) https://orcid.org/0000-0002-9663-3384
H. Dénes https://orcid.org/0000-0002-9214-8613
D. Kleiner https://orcid.org/0000-0002-7573-555X
Bärbel S. Koribalski https://orcid.org/0000-0003-4351-993X
S-H. Oh https://orcid.org/0000-0002-5648-9920
J. Rhee https://orcid.org/0000-0001-8496-4306
K. Spekkens https://orcid.org/0000-0002-0956-7949
O. I. Wong https://orcid.org/0000-0002-2504-7628
K. Bekki https://orcid.org/0000-0001-6163-4726
F. Bigiel https://orcid.org/0000-0003-0166-9745
H. M. Courtois https://orcid.org/0000-0003-0509-1776
B. W. Holwerda https://orcid.org/0000-0002-4884-6756
Kristen B. W. McQuinn https://orcid.org/0000-0001-5538-2614
J. M. van der Hulst https://orcid.org/0000-0002-9316-763X
L. Verdes-Montenegro https://orcid.org/0000-0003-0156-6180

References

Abadi, M. G., Moore, B., & Bower, R. G. 1999, MNRAS, 308, 947
Abramson, A., Kenney, J. D. P., Crowl, H. H., et al. 2011, AJ, 141, 164
Ayromlou, M., Kauffmann, G., Yates, R. M., et al. 2021, MNRAS, in press
Bahé, Y. M., & McCarthy, I. G. 2015, MNRAS, 447, 969
Bahé, Y. M., McCarthy, I. G., Balogh, M. L., et al. 2013, MNRAS, 430, 3017
Bahé, Y. M., Schaye, J., Barnes, D. J., et al. 2019, MNRAS, 485, 2287
Bekki, K. 2014, MNRAS, 438, 444
Bekki, K., Owers, M. S., & Couch, W. J. 2010, ApJL, 718, L27
Bigiel, F., Leroy, A., Walter, F., et al. 2008, AJ, 136, 2846
Blumenthal, K. A., & Barnes, J. E. 2018, MNRAS, 479, 3952
Boselli, A., & Gavazzi, G. 2006, PASP, 118, 517
Boselli, A., Roehlly, Y., Fossati, M., et al. 2016, A&A, 596, A11
Boselli, A., Voyer, E., Boissier, S., et al. 2014, A&A, 570, A69
Byrd, G., & Valtonen, M. 1990, ApJ, 350, 89
Catinella, B., Saintonge, A., Janowiecki, S., et al. 2018, MNRAS, 476, 875
Cayatte, V., van Gorkom, J. H., Balkowski, C., et al. 1990, AJ, 100, 604
Chabrier, G. 2003, PASP, 115, 763
Chen, H., Sun, M., Yagi, M., et al. 2020, MNRAS, 496, 4654
Chung, A., van Gorkom, J. H., Kenney, J. D. P., et al. 2007, ApJL, 659, L115
Chung, A., van Gorkom, J. H., Kenney, J. D. P., et al. 2009, AJ, 138, 1741
Cortese, L., Catinella, B., Boissier, S., et al. 2011, MNRAS, 415, 1797
Cortese, L., & Hughes, T. M. 2009, MNRAS, 400, 1225
Cortese, L., Minchin, R. F., Auld, R. R., et al. 2008, MNRAS, 383, 1519
Cowie, L. L., & McKee, C. F. 1977, ApJ, 211, 135
Crowl, H. H., Kenney, J. D. P., van Gorkom, J. H., et al. 2005, AJ, 130, 65
Cybulski, R., Yun, M. S., Fazio, G. G., et al. 2014, MNRAS, 439, 3564
De Lucia, G., Hirschmann, M., & Fontanot, F. 2019, MNRAS, 482, 5041
De Lucia, G., Weinmann, S., Poggianti, B. M., et al. 2012, MNRAS, 423, 1277
Dénes, H., Kilborn, V. A., & Koribalski, B. S. 2014, MNRAS, 444, 667

Eckert, D., Molendi, S., & Paltani, S. 2011, A&A, 526, A79
Elagali, A., Staveley-Smith, L., Rhee, J., et al. 2019, MNRAS, 487, 2797
Ettori, S. 2015, MNRAS, 446, 2629
Evrard, A. E., Bialek, J., Busha, M., et al. 2008, ApJ, 672, 122
Fitchett, M., & Merritt, D. 1988, ApJ, 335, 18
For, B.-Q., Staveley-Smith, L., Westmeier, T., et al. 2019, MNRAS, 489, 5723
Fujita, Y. 2004, PASJ, 56, 29
Gallagher, J. S. 1978, ApJ, 223, 386
Gavazzi, G. 1989, ApJ, 346, 59
Gavazzi, G., O'Neil, K., Boselli, A., et al. 2006, A&A, 449, 929
Gunn, J. E., & Gott, J. R. 1972, ApJ, 176, 1
Haines, C. P., Pereira, M. J., Smith, G. P., et al. 2013, ApJ, 775, 126
Haines, C. P., Pereira, M. J., Smith, G. P., et al. 2015, ApJ, 806, 101
Haynes, M. P., Giovanelli, R., Kent, B. R., et al. 2018, ApJ, 861, 49
Haynes, M. P., Giovanelli, R., Martin, A. M., et al. 2011, AJ, 142, 170
Hess, K. M., Jarrett, T. H., Carignan, C., et al. 2015, MNRAS, 452, 1617
Hess, K. M., & Wilcots, E. M. 2013, AJ, 146, 124
Huang, S., Haynes, M. P., Giovanelli, R., et al. 2012, ApJ, 756, 113
Jáchym, P., Köppen, J., Palouš, J., et al. 2009, A&A, 500, 693
Jaffé, Y. L., Poggianti, B. M., Moretti, A., et al. 2018, MNRAS, 476, 4753
Jaffé, Y. L., Smith, R., Candlish, G. N., et al. 2015, MNRAS, 448, 1715
Jaffé, Y. L., Verheijen, M. A. W., Haines, C. P., et al. 2016, MNRAS, 461, 1202
Jones, M. G., Papastergis, E., Haynes, M. P., et al. 2016, MNRAS, 457, 4393
Jung, S. L., Choi, H., Wong, O. I., et al. 2018, ApJ, 865, 156
Kapferer, W., Kronberger, T., Ferrari, C., et al. 2008, MNRAS, 389, 1405
Kauffmann, G., Heckman, T. M., White, S. D. M., et al. 2003, MNRAS, 341, 54
Kenney, J. D. P., Geha, M., Jáchym, P., et al. 2014, ApJ, 780, 119
Kenney, J. D. P., van Gorkom, J. H., & Vollmer, B. 2004, AJ, 127, 3361
Kleiner, D., Koribalski, B. S., Serra, P., et al. 2019, MNRAS, 488, 5352
Koribalski, B. S. 2020b, IAU Symp. 355, The Realm of the Low-Surface-Brightness Universe Proc., 2020, ed. Valls-Gabaud D., Trujillo I., Okamoto S., arXiv:2002.07312
Koribalski, B. S., Staveley-Smith, L., Westmeier, T., et al. 2020a, Ap&SS, 365, 118
Kourkchi, E., & Tully, R. B. 2017, ApJ, 843, 16
Larson, R. B., Tinsley, B. M., & Caldwell, C. N. 1980, ApJ, 237, 692
Lee, B., Chung, A., Tonnesen, S., et al. 2017, MNRAS, 466, 1382
Lee, J., Kimm, T., Katz, H., et al. 2020, ApJ, 905, 31
Lee-Waddell, K., Koribalski, B. S., Westmeier, T., et al. 2019, MNRAS, 487, 5248
Lima-Dias, C., Monachesi, A., Torres-Flores, S., et al. 2021, MNRAS, 500, 1323
Łokas, E. L. 2020, A&A, 638, A133
Lotz, M., Remus, R.-S., Dolag, K., et al. 2019, MNRAS, 488, 5370
Luo, Y., Kang, X., Kauffmann, G., et al. 2016, MNRAS, 458, 366
Maddox, N., Hess, K. M., Obreschkow, D., et al. 2015, MNRAS, 447, 1610
Mahajan, S., Mamon, G. A., & Raychaudhury, S. 2011, MNRAS, 416, 2882
Maier, C., Ziegler, B. L., Haines, C. P., et al. 2019, A&A, 621, A131
Markevitch, M., & Vikhlinin, A. 2007, PhR, 443, 1
McGaugh, S. S., Schombert, J. M., Bothun, G. D., et al. 2000, ApJL, 533, L99
McMahon, P. M., Richter, O.-G., van Gorkom, J. H., et al. 1990, in Second Wyoming Conf., The Interstellar Medium in External Galaxies, 3084, ed. D. J. Hollenbach & H. A. Thronson Jr. (Washington, DC: NASA), 217
McMahon, P. M., van Gorkom, J. H., Richter, O.-G., et al. 1992, AJ, 103, 399
McPartland, C., Ebeling, H., Roediger, E., et al. 2016, MNRAS, 455, 2994
Merritt, D. 1983, ApJ, 264, 24
Meyer, M. J., Zwaan, M. A., Webster, R. L., et al. 2004, MNRAS, 350, 1195
Moore, B., Katz, N., Lake, G., et al. 1996, Natur, 379, 613
Moore, B., Lake, G., & Katz, N. 1998, ApJ, 495, 139
Moreno, J., Torrey, P., Ellison, S. L., et al. 2019, MNRAS, 485, 1320
Moretti, A., Paladino, R., Poggianti, B. M., et al. 2020, ApJL, 897, L30
Muzzin, A., van der Burg, R. F. J., McGee, S. L., et al. 2014, ApJ, 796, 65
Navarro, J. F., Frenk, C. S., & White, S. D. M. 1997, ApJ, 490, 493
Nulsen, P. E. J. 1982, MNRAS, 198, 1007
Odekon, M. C., Koopmann, R. A., Haynes, M. P., et al. 2016, ApJ, 824, 110
Oman, K. A., Bahé, Y. M., Healy, J., et al. 2021, MNRAS, 501, 5073
Oman, K. A., & Hudson, M. J. 2016, MNRAS, 463, 3083
Paccagnella, A., Vulcani, B., Poggianti, B. M., et al. 2016, ApJL, 816, L25
Patton, D. R., Wilson, K. D., Metrow, C. J., et al. 2020, MNRAS, 494, 4969
Putman, M. E., Peek, J. E. G., & Joung, M. R. 2012, ARA&A, 50, 491
Ramos-Martínez, M., Gómez, G. C., & Pérez-Villegas, Á 2018, MNRAS, 476, 3781
Rasmussen, J., Mulchaey, J. S., Bai, L., et al. 2012, ApJ, 757, 122
Reiprich, T. H., & Böhringer, H. 2002, ApJ, 567, 716
Reynolds, T. N., Westmeier, T., Elagali, A., et al. 2021, MNRAS, 505, 1891
Rhee, J., Smith, R., Choi, H., et al. 2020, ApJS, 247, 45
Roediger, E., & Brüggen, M. 2006, MNRAS, 369, 567
Roediger, E., & Brüggen, M. 2007, MNRAS, 380, 1399
Roediger, E., Brüggen, M., Simionescu, A., et al. 2011, MNRAS, 413, 2057
Ruggiero, R., Machado, R. E. G., Roman-Oliveira, F. V., et al. 2019, MNRAS, 484, 906
Schmidt, T. M., Bigiel, F., Klessen, R. S., et al. 2016, MNRAS, 457, 2642
Scott, T. C., Bravo-Alfaro, H., Brinks, E., et al. 2010, MNRAS, 403, 1175
Scott, T. C., Brinks, E., Cortese, L., et al. 2018, MNRAS, 475, 4648
Serra, P., Jurek, R., & Flöer, L. 2012, PASA, 29, 296
Serra, P., Westmeier, T., Giese, N., et al. 2015, MNRAS, 448, 1922
Solanes, J. M., Manrique, A., García-Gómez, C., et al. 2001, ApJ, 548, 97
Steinhauser, D., Schindler, S., & Springel, V. 2016, A&A, 591, A51
Stevens, A. R. H., & Brown, T. 2017, MNRAS, 471, 447
Stevens, A. R. H., Diemer, B., Lagos, C., et al. 2019, MNRAS, 490, 96
Stevens, A. R. H., Diemer, B., Lagos, C., et al. 2019, MNRAS, 483, 5334
Stevens, A. R. H., Lagos, C., del, P., et al. 2020, MNRAS, 502, 3158
Tonnesen, S. 2019, ApJ, 874, 161
Tonnesen, S., & Bryan, G. L. 2008, ApJL, 684, L9
Tonnesen, S., & Bryan, G. L. 2009, ApJ, 694, 789
Tonnesen, S., & Bryan, G. L. 2010, ApJ, 709, 1203
Tonnesen, S., & Stone, J. 2014, ApJ, 795, 148
Verdes-Montenegro, L., Sulentic, J., Lisenfeld, U., et al. 2005, A&A, 436, 443
Vollmer, B., Cayatte, V., Balkowski, C., et al. 2001, ApJ, 561, 708
Vollmer, B., Soida, M., Beck, R., et al. 2013, A&A, 553, A116
Vollmer, B., Wong, O. I., Braine, J., et al. 2012, A&A, 543, A33
Wang, J., Catinella, B., Saintonge, A., et al. 2020a, ApJ, 890, 63
Wang, J., Koribalski, B. S., Jarrett, T. H., et al. 2017, MNRAS, 472, 3029
Wang, J., Koribalski, B. S., Serra, P., et al. 2016, MNRAS, 460, 2143
Wang, J., Xu, W., Lee, B., et al. 2020b, ApJ, 903, 103
Wang, J., Zheng, Z., D'Souza, R., et al. 2018, MNRAS, 479, 4292
Warmels, R. H. 1988, A&AS, 72, 427
Waters, C. Z., Magnier, E. A., Price, P. A., et al. 2020, ApJS, 251, 4
Wetzel, A. R., Tinker, J. L., Conroy, C., et al. 2013, MNRAS, 432, 336
Whiting, M. T. 2020, in ASP Conf. Ser. 522, Astronomical Data Analysis Software and Systems XXVII, 522 (San Francisco, CA: ASP), 469
Woo, J., Dekel, A., Faber, S. M., et al. 2013, MNRAS, 428, 3306
Xie, L., De Lucia, G., Hirschmann, M., et al. 2020, MNRAS, 498, 4327
Yoon, H., Chung, A., Smith, R., et al. 2017, ApJ, 838, 81
Yun, K., Pillepich, A., Zinger, E., et al. 2019, MNRAS, 483, 1042
Zhang, W., Li, C., Kauffmann, G., et al. 2013, MNRAS, 429, 2191
Zibetti, S., Charlot, S., & Rix, H.-W. 2009, MNRAS, 400, 1181